

# Combining experiments on luminescent centres in hexagonal boron nitride with the polaron model and *ab initio* methods towards the identification of their microscopic origin

Moritz Fischer,<sup>1,2,3</sup> Ali Sajid,<sup>2,4</sup> Jake Iles-Smith,<sup>5</sup> Alexander Hötger,<sup>6</sup> Denys I. Miakota,<sup>1</sup> Mark K. Svendsen,<sup>4</sup> Christoph Kastl,<sup>6</sup> Stela Canulescu,<sup>1</sup> Sanshui Xiao,<sup>1,2,3</sup> Martijn Wubs,<sup>1,2,3</sup> Kristian S. Thygesen,<sup>2,4</sup> Alexander W. Holleitner,<sup>6</sup> and Nicolas Stenger<sup>1,2,3,\*</sup>

<sup>1</sup>*Department of Electrical and Photonics Engineering, Technical University of Denmark, 2800 Kgs. Lyngby, Denmark*

<sup>2</sup>*Centre for Nanostructured Graphene, Technical University of Denmark, 2800 Kgs. Lyngby, Denmark*

<sup>3</sup>*NanoPhoton - Center for Nanophotonics, Technical University of Denmark, 2800 Kgs. Lyngby, Denmark*

<sup>4</sup>*Department of Physics, Technical University of Denmark, 2800 Kgs. Lyngby, Denmark*

<sup>5</sup>*Department of Electrical and Electronic Engineering, The University of Manchester, Sackville Street Building, Manchester M1 3BB, United Kingdom*

<sup>6</sup>*Walter Schottky Institute and Physics Department, Technical University of Munich, 85748 Garching, Germany*

The two-dimensional material hexagonal boron nitride (hBN) hosts luminescent centres with emission energies of  $\sim 2$  eV which exhibit pronounced phonon sidebands. We investigate the microscopic origin of these luminescent centres by combining *ab initio* calculations with non-perturbative open quantum system theory to study the emission and absorption properties of 26 defect transitions. Comparing the calculated line shapes with experiments we narrow down the microscopic origin to three carbon-based defects:  $C_2C_B$ ,  $C_2C_N$ , and  $V_N C_B$ . The theoretical method developed enables us to calculate so-called photoluminescence excitation (PLE) maps, which show excellent agreement with our experiments. The latter resolves higher-order phonon transitions, thereby confirming both the vibronic structure of the optical transition and the phonon-assisted excitation mechanism with a phonon energy  $\sim 170$  meV. We believe that the presented experiments and polaron-based method accurately describe luminescent centres in hBN and will help to identify their microscopic origin.

**Keywords:** *luminescent centres, hexagonal boron nitride, polaron formalism, photoluminescence excitation, excitation mechanism*

## INTRODUCTION

Luminescent centres in hexagonal boron nitride (hBN) have gained an increased scientific interest due to the demonstration of single photon emission with a brightness comparable to semiconductor quantum dots [1]. These luminescent centres emit at photon energies around 2 eV and persist even at room temperature [2], making hBN a promising material to realise future optoelectronic technologies such as quantum telecommunication [3, 4] and quantum sensing [5].

The microscopic origin of 2 eV luminescent centres in hBN has been experimentally narrowed down to carbon-based defects by bottom-up and post-growth techniques [6], however the atomic structure of the underlying defect remains elusive. One subset of 2 eV luminescent centres are group I centres [7] with pronounced phonon side bands (PSB). The chemical composition of the defect will naturally alter the mechanical vibrations of the crystal which will in-turn modify the structure of the PSB observed in photoluminescence. This motivates the comparison of experimental lineshapes with those obtained via *ab initio* methods [8–10].

A typical approach to calculating the photoluminescence of defect transitions is to first calculate the elec-

tronic structure and phonon modes using *ab initio* methods, before using this information to calculate the photoluminescence spectrum with the generating function approach [8–14]. Whilst this method can calculate the linear absorption and emission spectra with atomistic precision, it cannot resolve coherent dynamics between electronic states of the defect transition, and is limited to unstructured electromagnetic environments. As the field strives towards coherent control of hBN luminescent centres [15], and interfacing emitters with plasmonic [16] and photonic structures [17], new theoretical methods are required to describe the behaviour of defect complexes.

In this joint experiment-theory investigation, we study the photoluminescence and photoluminescence emission (PLE) of 2 eV luminescent centres in hBN. We combine a non-perturbative master equation treatment of electron-phonon interaction with *ab initio* methods to calculate the photoluminescence line shapes of 26 candidate defect transitions. This methodology, based on the polaron formalism [18], maintains the atomistic accuracy of the generating function approach, while allowing to simulate PLE maps of the studied defect transition by taking into account external driving fields. By comparing the calculated photoluminescence against measurements for twelve group I centres we exclude all but three candidate defects: the neutral substitutional carbon trimers  $C_2C_B$  and  $C_2C_N$  as well as  $V_N C_B$ . Here,  $C_2C_B$  and  $C_2C_N$  are shorthand notations of  $C_B C_N C_B$  and  $C_N C_B C_N$ , re-

\* Corresponding author. Email: niste@dtu.dk

spectively. By comparing measured and theoretical PLE, which may be calculated directly using the polaron formalism, we are able to resolve higher-order phonon transitions. By studying the emission of zero-phonon line (ZPL) and PSB simultaneously, we confirm that the excitation mechanism in group I emitters is phonon-assisted with a phonon energy of  $\sim 170$  meV. The combination of theoretical and experimental methods presented here will help to identify the microscopic origin of luminescent centres in hBN.

## RESULTS AND DISCUSSION

To generate luminescent centres in hBN we use a process that was developed recently in our group [7]. Briefly, we irradiate high-quality multilayer hBN with oxygen atoms and use subsequent annealing to achieve high densities of luminescent centres emitting at photon energies around 2 eV. In our previous work, we carried out room-temperature characterisation of group I and group II centres, as defined in Ref. [7]. In the work presented here, we focus our attention on low-temperature characterisation of group I centres which show a specific line shape with pronounced PSB at ZPL detunings around 170 meV, as observed also in other works [19–21]. Furthermore, these group I centres emit at photon energies around 2 eV just like single-photon emitters in hBN [2]. In this work, we define luminescent centres as experimental line shapes while theoretical line shapes are called defect transitions. Single-photon emitters are luminescent centres with an auto-correlation function fulfilling the criterion  $g^{(2)}(0) < 0.5$ . In the following we will study luminescent centres with a focus on group I line shapes.

Fig. 1a shows the photoluminescence of a group I centre at room and low temperature. Decreasing the temperature results in a narrower ZPL and reveals a detailed structure of the PSB. When comparing photoluminescence line shapes for different group I centres at low temperature, we find variations among the PSB line shapes as shown in Supplementary Information I. These differences correspond to variations in the electron-phonon coupling of the defect transition among the luminescent centres, and may be due to different underlying defects. It is therefore necessary to compare several different defect transitions to *individual* luminescent centres, as outlined below. This is in contrast to comparing total Huang-Rhys factors of several defect transitions with experiments, which neglects the detailed information about the spectral structure of the PSB.

### Screening of defect transitions

To get insight into the microscopic origin of 2 eV luminescent centres in hBN, we study 26 different defect transitions. We focus on carbon-based defects as these have been experimentally demonstrated to be responsible for luminescent centers emitting around 2 eV [6]. Furthermore, our generation process can easily generate carbon-based defects by incorporating ubiquitous hydrocarbons

from the annealing environment as well as by carbon impurities intrinsically present in the hBN [7]. We note that we use the PBE functional for this screening of defect transitions while the HSE06 functional is used for a more accurate study of a selected subset of defect transitions.

To obtain the theoretical photoluminescence line shapes, we use *ab initio* methods to calculate the ZPL energies and partial Huang-Rhys factors of all studied defect transitions (see Supplementary Information II). With these Huang-Rhys factors at hand, we can construct the spectral density [23]

$$J_{\text{Sim}}(\omega) = \sum_k s_k \delta(\omega_k - \omega) \quad (1)$$

Here,  $\omega$  is the angular frequency and  $s_k$  the partial Huang-Rhys factor associated to a phonon mode of angular frequency  $\omega_k$ . To account for the natural lifetime of phonons, we approximate the  $\delta$ -functions with Gaussian functions as outlined in Supplementary Information III. For details on the *ab initio* simulations, we refer the reader to the Methods.

With the spectral density at hand, we can calculate the dynamics and optical properties of the system using the polaron method. Here, the electronic states of the defect transition are dressed by vibrational modes of the phonon environment [18, 24]. This enables one to derive a quantum master equation that is non-perturbative in the electron-phonon coupling strength, and thus captures phonon sideband processes in the photoluminescence [24, 25]. In Fig. 1b we compare the photoluminescence of Emitter A against the line shape for the carbon trimer  $\text{C}_2\text{C}_\text{B}$ , calculated using the polaron theory. The black bars show the partial Huang-Rhys factors ( $s_k$ ) illustrating the origin of the phonon side bands from *ab initio* methods. We highlight that the line shape of  $\text{C}_2\text{C}_\text{B}$  is unique for Emitter A since we fit each theoretical line shape to *individual* experimental line shapes, with the ZPL linewidth as the only free fitting parameter (see Supplementary Information III).

In order to screen the 26 different defect transitions calculated with *ab initio* methods, we calculate the photoluminescence mean  $\langle S \rangle$  and variance  $\sigma$ , defined as,

$$\langle S \rangle = \frac{1}{N} \sum_{i=1}^N S(\Delta_i), \quad \sigma^2 = \frac{1}{N} \sum_{i=1}^N (S(\Delta_i) - \langle S \rangle)^2,$$

where  $S(\Delta_i)$  is the intensity of the spectrum at the ZPL detuning  $\Delta_i$ , and  $N$  is the number of data points (see Methods). If the photoluminescence mean and variance of a defect transition are close to the experimental values, the theoretical photoluminescence line shape is similar to the experimental one, thus providing a coarse approach to screening relevant defect transitions.

As an example, we apply this method to Emitter A and plot the photoluminescence mean and variance for all calculated defect transitions along with the experimental

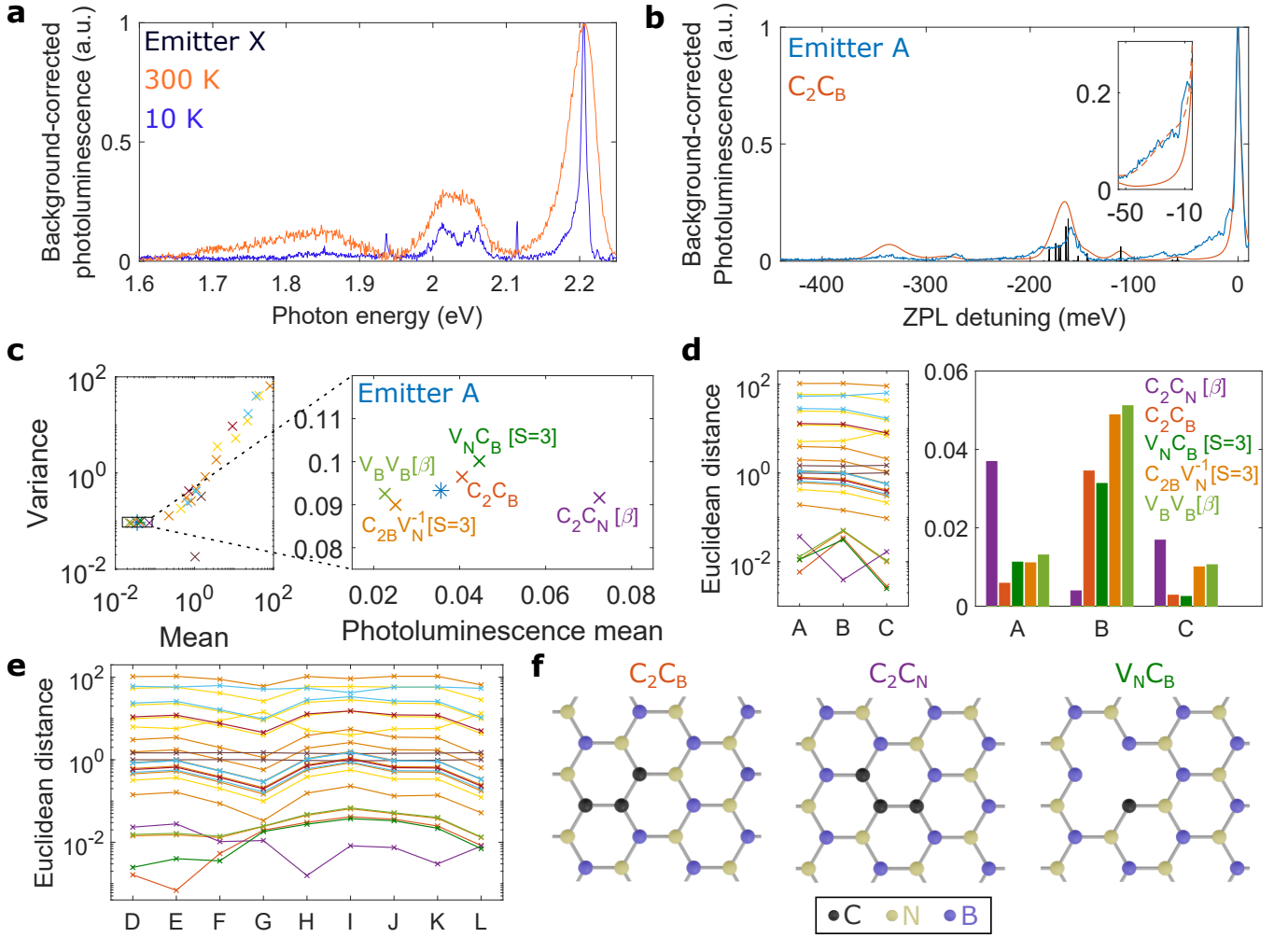


FIG. 1. **Screening of defect transitions.** (a) Room- and low-temperature spectra of Emitter X under 2.37 eV excitation. a.u., arbitrary units. (b) Comparison of low-temperature photoluminescence of Emitter A (under 2.321 eV excitation) with the theoretical emission line shape of  $C_2C_B$  using the PBE functional (without acoustic phonons). The black bars show the partial Huang-Rhys factors (a.u.) obtained with the PBE functional. The inset shows the theoretical line shape of  $C_2C_B$  using the HSE06 functional with and without acoustic phonons in dashed and solid lines, respectively. (c) Scatter plot comparing the photoluminescence mean and variance of theoretically calculated defect line shapes with the experimental data of Emitter A. The most likely defect transitions are shown in the right panel which is the region close to the experimental data, marked by the square in the left panel. (d) Euclidean distances of all defect transitions in corresponding colors to (c) for Emitter A, B and C. The histogram on the right shows the distances for the five most likely defect candidates. (e) Euclidean distances for Emitter D to L in corresponding colors to (c). All emitters show small distances for the same five defect transitions. (f) Schematics of  $C_2C_B$ ,  $C_2C_N$ , and  $V_N C_B$  where the latter is taken from Ref. [22]. All experimental photoluminescence line shapes are background-corrected as outlined in Supplementary Information V. We note that the PBE functional is used for all defect transitions (including  $C_2C_B$ ,  $C_2C_N[\beta]$ , and  $V_N C_B[S=3]$ ), except for the inset in (b) where the HSE06 functional is used.

values (Fig. 1c). Here, different colors correspond to different defects, some of which have several optically active transitions (details in Supplementary Information IV). The scatter plot (in double logarithmic scale) shows that the photoluminescence mean and variance for most defect transitions differ significantly from the experimental data and thus are unlikely candidates, while the most likely defect transitions are clustered around the experimental data of Emitter A, as shown in the right panel of Fig. 1c.

Inspired by work on Raman spectroscopy [26], we define an Euclidean distance  $d$  to the experiment

$$d = \sqrt{(\langle S \rangle - \langle E \rangle)^2 + (\sigma - s_E)^2},$$

where,  $\langle E \rangle$  and  $s_E$  are the experimental mean and variance while  $\langle S \rangle$  and  $\sigma$  are the mean and variance for each defect transition. For Emitter A, the line shape of  $C_2C_B$  is very similar to the experiments, thus  $C_2C_B$  is located closely to the experiment in the scatter plot (Fig. 1c) and

shows a small Euclidean distance (Fig. 1d in logarithmic scale).

The scatter plot shown in Fig. 1c depends on the luminescent centre studied, since the ZPL line width differs among luminescent centres. Therefore, we calculate an *individual* scatter plot for each luminescent centre (for Emitter B and C these are given in Supplementary Information IV) with the resulting Euclidean distances shown along with Emitter A in Fig. 1d. We find that the same five defect transitions show similar photoluminescence line shapes for Emitter A, B and C. Expanding our analysis to twelve group I centres (line shapes shown in Supplementary Information I), we find that for all experiments the five closest defect transitions are identical to the ones for Emitter A (Fig. 1e). Therefore, we focus our attention on these five defect transitions while discarding the other 21 transitions.

### Second screening step

The statistical analysis described above is independent on the theoretical ZPL energy because we match the theoretical line shapes with the experimental ZPL energies. Thus, comparing theoretical with experimental ZPL energies can help to narrow down the microscopic origin even further. For twelve group I centres the experimental ZPL energies are between 2.0 and 2.3 eV (see Tab. I) and thus theoretical ZPL energies much different to this range reveal less likely candidates. Among the five defect transitions showing small Euclidean distances to these twelve centres (Fig. 1), we neglect  $V_B V_B[\beta]$  and  $C_{2B} V_N^{-1}[S=3]$  since their predicted ZPL energies are too high and too low, respectively (see Tab. I). On the contrary, the ZPL energies of  $C_2 C_B$ ,  $C_2 C_N[\beta]$ , and  $V_N C_B[S=3]$  are similar to the experiments as shown in Tab. I. In the following, we call these three defects  $C_2 C_B$ ,  $C_2 C_N$ , and  $V_N C_B$ . The ZPL energies of these three defects show good agreement with experiments, while even the relatively more accurate HSE06 functional shows slightly smaller energies compared to the experimental values.

All in all, we can exclude 23 defect transitions for twelve group I centres and identified three most likely candidates:  $C_2 C_B$ ,  $C_2 C_N$ , and  $V_N C_B$ . Fig. 1f shows the schematics of these three defect transitions. We note that  $V_N C_B$  needs a nearby defect to populate the ground state, because the intersystem crossing from the singlet state can be neglected at our experimental detunings (see Supplementary Information VI).

### PLE spectroscopy

In contrast to the generating function approach, our polaron formalism allows to introduce an external driving field in the system Hamiltonian, thereby directly simulating PLE experiments. For the latter, the photoluminescence is measured as a function of laser detuning which is defined as the laser energy minus the ZPL energy of the studied luminescent centre.

Fig. 2a shows the experimental PLE data (in logarithmic scale) of Emitter A, i.e. the photoluminescence as a function of laser detuning (details and further group I centres in Supplementary Information VII and VIII).

Defect transition	PBE	HSE06	Experiments
$C_2 C_B$	1.16 eV	1.36 eV	2.0 - 2.3 eV
$C_2 C_N[\beta]$	1.51 eV	1.67 eV	
$V_N C_B[S=3]$	1.39 eV	1.75 eV	
$V_B V_B[\beta]$	2.70 eV	–	
$C_{2B} V_N^{-1}[S=3]$	0.90 eV	–	

TABLE I. **Theoretical and experimental ZPL energies.** The applied functional (PBE or HSE06) for the calculations of the defect transitions is given by the column name while the range of ZPL energies of Emitter A to L are shown in the rightmost column (details in Supplementary Information I). We did not use the HSE06 functional for  $V_B V_B[\beta]$  and  $C_{2B} V_N^{-1}[S=3]$  since their PBE results are very different to the experimental ZPL energies. The spin minority channel is labelled by  $\beta$  and  $S=3$  denotes the triplet state while we suppress the notations for spin majority channel and other spin states (details in Supplementary Information II).

The ZPL emission at photon energies around 2.15 eV is strong at a detuning of 168 meV and shows intermediate strength at 341 meV detuning. Moreover, the PSB emission around 1.99 eV is enhanced at the same laser detunings. In particular, the enhanced PSB emission at 341 meV detuning (highlighted by the white box) shows strong evidence of a phonon-assisted mechanism, as outlined below.

To model the PLE results precisely, we use the relatively more accurate HSE06 functional and study the photoluminescence line shape of Emitter A in more detail. The experimental and theoretical line shape disagree at ZPL detunings from 10 to 50 meV, as shown by the inset of Fig. 1b. While this spectral range was previously associated with another, independent electronic transition [27], we assign this range to a low-energy, acoustic PSB from the *same* electronic transition since its PLE characteristic shows excellent qualitative agreement with the ZPL (see Supplementary Information IX).

The experimentally observed acoustic PSB is not reproduced by our *ab initio* calculations, since the latter are carried out in a perfectly planar system with high symmetry that exhibits vanishing coupling to acoustic phonons, i.e. the corresponding partial Huang-Rhys factors are zero. This is in contrast to our experiments where the symmetry can be broken by local strain, non-radiative defects close by, non-parallel hBN layers as well as the vicinity of edges, kinks, and grain boundaries. Such a symmetry breaking allows the coupling to acoustic phonons which we observe in several experimental photoluminescence line shapes as asymmetric ZPL lines (see Supplementary Information I). We highlight that the asymmetric ZPL observed in our experiments has been reported in several works on group I centres [6, 7, 28–31] independent on the generation process.

To account for the aforementioned coupling to acoustic phonons, we modify the spectral density shown in Equation (1). We include acoustic phonons by adding a Gaussian contribution such that the total spectral density is

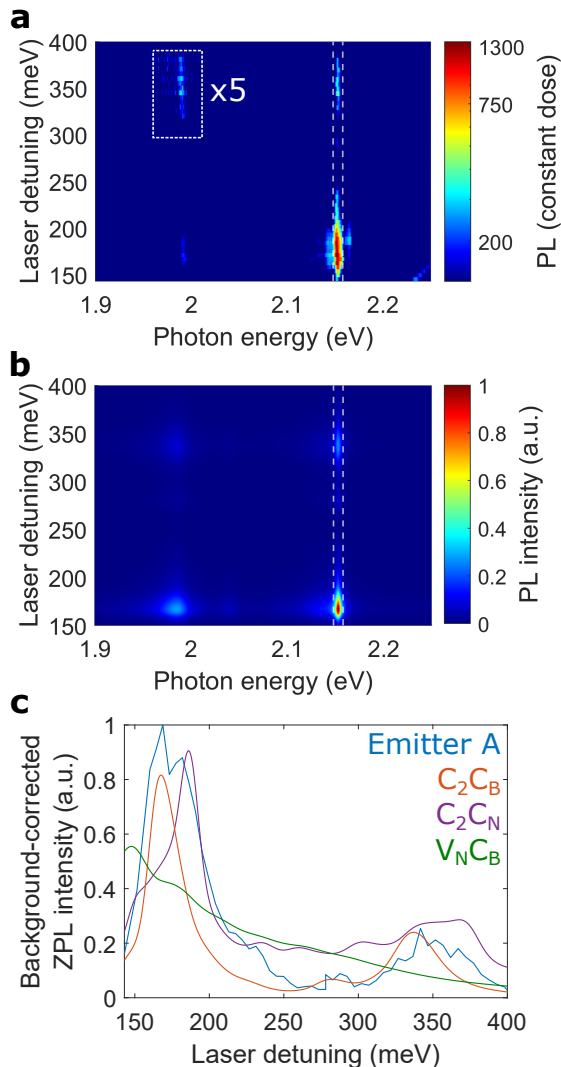


FIG. 2. **PLE spectroscopy.** (a) Experimental PLE map of Emitter A at 10K, background corrected as outlined in Supplementary Information IX. The photoluminescence (PL) in the highlighted box is multiplied by 5. The dim upward line in the bottom right corner corresponds to the silicon Raman  $\sim 520 \text{ cm}^{-1}$ . (b) Theoretical PLE map of  $\text{C}_2\text{C}_\text{B}$ , shifted to the experimental ZPL energy of 2.153 eV. Here, the HSE06 functional is used and acoustic phonons are included in the spectral density. (c) Comparison of the experimental ZPL intensity, indicated by dashed lines in (a) and (b), with  $\text{C}_2\text{C}_\text{B}$ ,  $\text{C}_2\text{C}_\text{N}$ , and  $\text{V}_\text{N}\text{C}_\text{B}$ . We note that the experimental ZPL intensity is rescaled to 170 meV and background-corrected as outlined in Supplementary Information IX. Furthermore, all theoretical curves include acoustic phonons as described in the main text.

written as  $J(\omega) = J_\text{Sim}(\omega) + J_\text{acoustic}(\omega)$  with

$$J_\text{acoustic}(\omega) = \alpha \omega_c^{-2} \omega \exp(-\omega^2/\omega_c^2),$$

where  $\alpha$  and  $\omega_c$  are found by fitting the photoluminescence spectrum. This form of spectral density is commonly used to describe the bulk acoustic phonons in three dimensions resulting from deformation potential coupling

observed in semiconductor quantum dots [18, 32]. We find that the experimental photoluminescence at small ZPL detunings is closely resembled by calculations that include acoustic phonons, showing a very precise theoretical description (see inset of Fig. 1b). We refer the reader to the Methods section for more details on the theory and the fitting procedure used.

With the total spectral density at hand, we calculate the complete PLE spectrum of several defect transitions. While the commonly-used generating function approach is limited to the comparison of photoluminescence line shapes, our polaron-based method allows to directly calculate the theoretical ZPL intensity by introducing an external driving field into the system Hamiltonian. For each laser detuning we calculate the ZPL intensity by sweeping out the experimental detuning range. We highlight that for the obtained ZPL intensities we use the phonons of the ground state, i.e. the identical phonons utilised for the emission line shape. To the best of our knowledge, this is the first time that PLE measurements of 2 eV luminescent centres in hBN are replicated by a theoretical model.

Fig. 2b shows the complete PLE map of  $\text{C}_2\text{C}_\text{B}$  while the maps of  $\text{C}_2\text{C}_\text{N}$  and  $\text{V}_\text{N}\text{C}_\text{B}$  are shown in Supplementary Information III. We find excellent agreement of the experimental PLE map with  $\text{C}_2\text{C}_\text{B}$  and  $\text{C}_2\text{C}_\text{N}$ , reflecting a very good match of both emission line shape as well as ZPL and PSB intensities. The theoretical PLE of  $\text{C}_2\text{C}_\text{B}$  shows a slightly stronger enhancement at 341 meV detuning compared to the experimental data. This may be due to other nonradiative decay channels like shelving states [20] which are not considered in our model.

To compare our PLE experiments with several defect transitions, we study the ZPL intensity which is defined as the area under the ZPL (indicated by vertical lines in Fig. 2a and b). Fig. 2c shows excellent agreement of the experimental ZPL intensity with  $\text{C}_2\text{C}_\text{B}$  and  $\text{C}_2\text{C}_\text{N}$  while  $\text{V}_\text{N}\text{C}_\text{B}$  shows poorer agreement, thus allowing us to exclude the latter defect for Emitter A.

All in all, our excellent agreement of the complete experimental PLE with our polaron-based calculations for  $\text{C}_2\text{C}_\text{B}$  and  $\text{C}_2\text{C}_\text{N}$  is outstanding compared to previous work [33]. This finding infers that, among the studied defect transitions,  $\text{C}_2\text{C}_\text{B}$  and  $\text{C}_2\text{C}_\text{N}$  are the most likely microscopic origins for Emitter A. We highlight that the generation mechanism of Emitter A, outlined in Ref. [7], also holds for  $\text{C}_2\text{C}_\text{B}$  and  $\text{C}_2\text{C}_\text{N}$ , since both defects can be formed by merging of  $\text{C}_\text{N}$  and  $\text{C}_\text{B}$  during thermal annealing.

Previously, experimental photoluminescence line shapes were compared with vacancies [2, 34], oxygen-based defects [35] and carbon-based defects [6–8]. Although Emitter A shows good agreement with  $\text{C}_2\text{C}_\text{B}$  and  $\text{C}_2\text{C}_\text{N}$ , other luminescent centres, also generated by our process, show agreement with different defects. One example is Emitter C (see Fig. 1d) showing a small Euclidean distance for  $\text{V}_\text{N}\text{C}_\text{B}$ , i.e. a good agreement with this defect. Furthermore, our irradiation-based

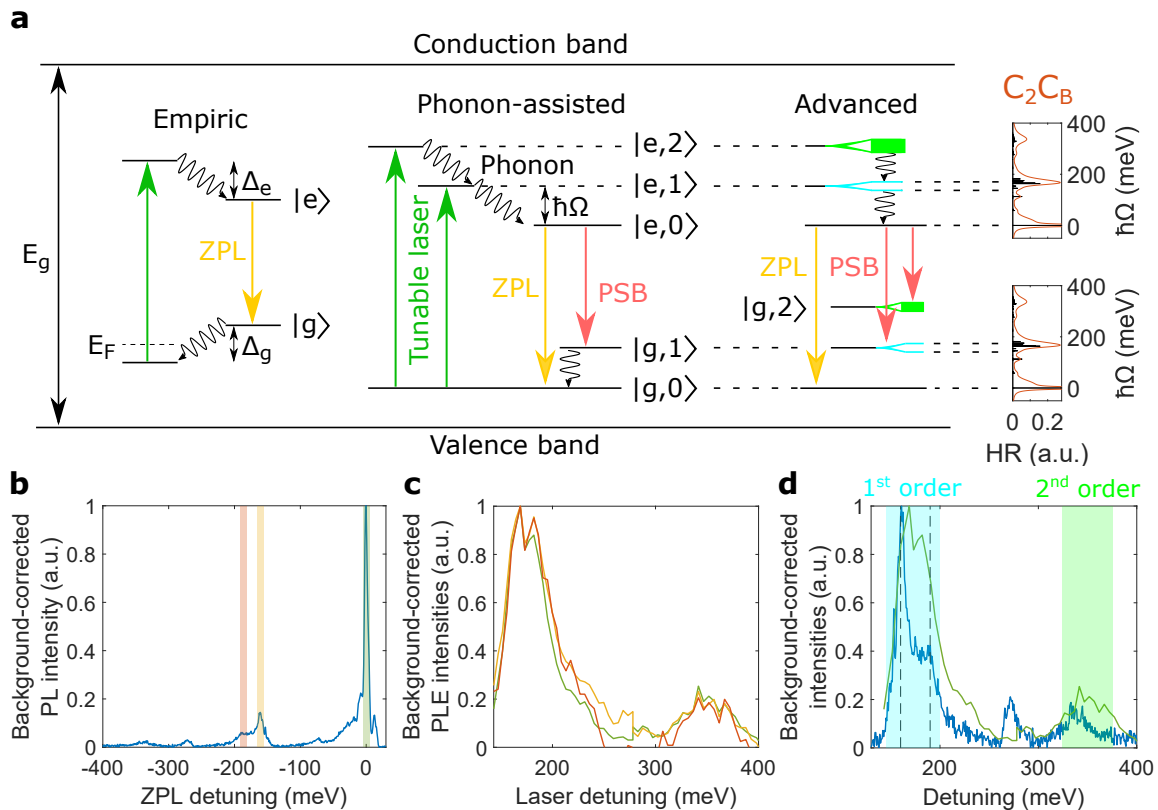


FIG. 3. **Excitation mechanism of Emitter A.** (a) Empiric, phonon-assisted, and advanced excitation mechanisms. The zero-phonon line (ZPL) and the phonon sidebands (PSB) are shown in yellow and red, respectively. The empiric mechanism has relaxation processes with energies  $\Delta_e$  and  $\Delta_g$  while the phonon-assisted mechanism shows relaxation via phonons with energy  $\hbar\Omega$ . Here, the excited states are labelled with  $|e, n\rangle$  corresponding to the electron in the excited state and its environment occupied by  $n$  phonons. The advanced mechanism is also phonon-assisted but with split first-order states  $|e, 1\rangle$  and  $|g, 1\rangle$ . The rightmost panel shows the partial Huang-Rhys factors (HR) and the photoluminescence line shape for  $C_2C_B$  in black and red, respectively. This photoluminescence line shape is obtained with the HSE06 functional and acoustic phonons. Further details are presented in the Methods. (b) The spectral ranges of two optical PSB are shaded in orange and yellow on top of the photoluminescence spectrum at 168 meV laser detuning. The bandwidth for the PSB intensities is 10 meV, identical to the one used for the ZPL intensity. The spectral range of the ZPL (green) is identical to the dashed lines in Fig. 2a. We assign the peak around 270 meV to another luminescent centre while the peak around 340 meV corresponds to the second-order PSB. (c) ZPL and PSB intensities in colors corresponding to (b). We highlight that the ZPL intensity is identical to Fig. 2c. (d) ZPL intensity in green and flipped photoluminescence in blue. The first- and second-order phonon states are shaded in colors corresponding to the advanced mechanism in (a). The vertical dashed lines are at detunings of 160 and 190 meV, respectively. We note that all photoluminescence (PL) and PLE intensities are background-corrected and normalised (see Supplementary Information V and IX).

process also generates luminescent centres with line shapes different to group I centres that show small Euclidean distances to defects different to  $C_2C_B$ ,  $C_2C_N$ , and  $V_N C_B$  (see Supplementary Information X). We are convinced that our process generates several types of defects that appear as 2 eV luminescent centres in our experiments. Therefore, comparing PLE maps of *individual* luminescent centres with our polaron method helps to identify their microscopic origins.

### Excitation mechanism

The microscopic origin of twelve group I centres has been narrowed down to three defect transitions (Fig. 1). These three transitions have relatively large Huang-Rhys factors around 170 meV and thus can be modelled as two-

level systems with discrete vibronic energy levels (see Supplementary Information II). To verify the vibronic structure of these energy levels, which are directly related to the excitation mechanism, PLE is a strong tool since it probes off-resonant transitions in both ground and excited states.

The excitation mechanism of 2 eV luminescent centres in hBN does not involve interband transitions since the photon energy of the excitation laser ( $\sim 2.5$  eV) is much smaller than the band gap  $E_g \sim 6$  eV [36]. Supported by charge transfer experiments [37], the excitation mechanism most likely involves only electronic states inside the band gap, so-called deep levels. This makes the energy of the driving laser very important since only few,

discrete electronic states are available - in contrast to a continuum of states for interband transitions in semiconductors.

For 2 eV luminescent centres in hBN, one possible configuration of these deep levels is the empiric mechanism illustrated in Fig. 3a. Here, the driving laser excites an electron from a deep level below the Fermi level  $E_F$  to another level lying far below the conduction band. From here, the electron relaxes to the excited state  $|e\rangle$  by dissipating energy  $\Delta_e$ . Then, a photon belonging to the ZPL is emitted by a transition to the ground state  $|g\rangle$ , followed by another relaxation with energy  $\Delta_g$ .

Recent PLE experiments [33, 38] observed an enhanced ZPL emission at detunings around 170 meV. While the authors assigned these results to a phonon-assisted process, the empiric mechanism can in principle also be the underlying excitation mechanism with  $\Delta_e + \Delta_g \sim 170$  meV. On the contrary, our PLE measurements show enhanced ZPL intensities both at detunings around 170 *and* 340 meV (see Fig. 2c). The empiric mechanism could be expanded by another electronic level, but the simplest explanation of our PLE results is the phonon-assisted excitation mechanism.

### Phonon-assisted mechanism

As shown above, our PLE measurements can not be explained by the empiric mechanism. Therefore, we introduce the phonon-assisted excitation mechanism, also called Huang-Rhys model (see Fig. 3a) which was proposed in previous works on hBN [33, 39]. Here, two electronic states couple to one phonon mode with energy  $\hbar\Omega$ , resulting in discrete vibronic energy levels  $|e, n\rangle$  and  $|g, m\rangle$ . The driving laser excites a high lying vibronic state  $|e, n\rangle$  in the excited electronic manifold which rapidly relaxes to its lowest state  $|e, 0\rangle$ . A photon is then emitted through an electronic transition to the ground-state manifold, producing ZPL and PSB emission.

By varying the photon energy of the driving laser, we can resonantly excite different vibronic states  $|e, n\rangle$  in the excited-state manifold (see Fig. 3a). In particular, the ZPL and PSB emission are enhanced at equally-spaced laser detunings of  $\hbar\Omega$  and  $2\hbar\Omega$ , also called one- and two-phonon detuning. We observe this in our PLE experiments by studying the ZPL intensity (see Fig. 2c) but also by studying two PSB intensities, as outlined below.

To study PSB emissions as a function of laser detuning, we define the PSB intensity as the area under the PSB, indicated by shaded areas in Fig. 3b. We find an excellent qualitative agreement of the ZPL intensity with the two PSB intensities that are taken at ZPL detunings of around 160 and 190 meV (see Fig. 3c). This finding shows that the ZPL and the two optical PSB have the same excitation mechanism and thus can be used to investigate the excitation mechanism of Emitter A. To the best of our knowledge, this is the first time that ZPL and PSB intensities of 2 eV luminescent centres in hBN are directly compared with each other.

The ZPL and PSB intensities are enhanced at equally-

spaced detunings of  $\sim 170$  and  $\sim 340$  meV, as shown in Fig. 3c. This experimental finding agrees excellently well for  $\hbar\Omega \sim 170$  meV with the phonon-assisted mechanism where ZPL and PSB emission are enhanced at detunings of  $\hbar\Omega$  and  $2\hbar\Omega$ . At detunings between the two aforementioned energies, we obtain small ZPL and PSB intensities because the excitation laser energy is between the two states  $|e, 1\rangle$  and  $|e, 2\rangle$ . Furthermore, the photoluminescence (Fig. 3b) shows first- and second-order PSB at detunings around 170 and 340 meV corresponding to optical transitions from  $|e, 0\rangle$  to  $|g, 1\rangle$  and  $|g, 2\rangle$ , respectively. Therefore, our experiments allow us to discard the empiric mechanism for Emitter A and confirm indications of a phonon-assisted mechanism for group I centres in hBN. This might pave the way towards a universal excitation mechanism, which could also explain other experimental findings such as high-temperature photoluminescence [40] and photophysics [20, 41].

In the phonon-assisted excitation mechanism (see Fig. 3a), the ZPL emission via  $|e, 2\rangle$  (two-phonon detuning) and the PSB emission via  $|e, 1\rangle$  (one-phonon detuning) are both processes involving two phonons, and thus should show comparable intensities (details in Methods). Indeed, our experimental ZPL intensity at two-phonon detuning shows similar strength as both PSB intensities at one-phonon detuning, since both processes involve two phonons (see Supplementary Information IX). Furthermore, the ZPL intensity via  $|e, 1\rangle$  involves only one phonon and thus is stronger than both aforementioned two-phonon processes. These results further support the phonon-assisted excitation mechanisms of Emitter A.

### Detailed phonon coupling

The experimental photoluminescence of Emitter A shows a first-order PSB at detunings around 170 meV which consists of two distinct peaks at 160 and 190 meV, shown by dashed lines in Fig. 3d. Furthermore, we find that the ZPL intensity also shows a strong peak at detunings around 170 meV with two shallower peaks at 160 and 190 meV. This reveals that both first-order states  $|e, 1\rangle$  and  $|g, 1\rangle$  are split into two distinct levels, reflected in the advanced excitation mechanism (see Fig. 3a). Here, the second-order phonon replicas  $|e, 2\rangle$  and  $|g, 2\rangle$  are shown as continua since our experiments do not show distinct peaks at two-phonon detuning (see Fig. 3d). The calculated HR factors of  $C_2C_B$  (Fig. 3a) as well as split first-order PSB of several group I centres (see Supplementary Information I) support that several phonon modes are involved in the excitation mechanism of group I centres in hBN. We note that previous works have assigned a split  $|g, 1\rangle$  to longitudinal and transverse optical bulk phonons [15, 19, 42]. In our work, we provide a more accurate description since we calculate the phonon modes coupled to the defect in the lattice, thereby taking into account both localised and delocalised phonon modes.

In Fig. 3d we compare the ZPL intensity with the flipped photoluminescence line shape. For the 160 and 190 meV peaks we observe a blueshift and a redshift between the photoluminescence and ZPL intensity, respec-

tively. This could point towards different phonon coupling between ground and excited states. While the redshift of the 190 meV peak is in agreement with previous work [38], the blueshift for the 160 meV peak has not been observed. Both spectral shifts (around 10 meV) are, however, on the same order of magnitude as the spectral resolution of both PLE setups (around 5 meV) and thus further PLE experiments with higher spectral resolution are needed to confirm the presence of fine differences in the phonon coupling between ground and excited states.

## CONCLUSION

In summary, we have studied the photoluminescence of luminescent centres in hBN with a focus on group I centres showing pronounced PSB around 170 meV and a ZPL energy around 2 eV. By combining *ab initio* methods with the non-perturbative polaron method, we calculated the emission line shapes of 26 different defect transitions. Studying both the theoretical ZPL energy and the Euclidean distance between experiment and theory showed that  $C_2C_B$ ,  $C_2C_N$ , and  $V_N C_B$  are the most likely defect candidates for twelve experimental line shapes. Our method of using the Euclidean distance represents a new tool to narrow down the number of possible defects responsible for luminescent centres in insulators as well as to make accurate predictions of their optical properties when integrated in photonic structures.

Our method of analysis represents a complement to the common methodology, which compares theoretical values of the total Huang-Rhys or Debye-Waller factor with values extracted from the experiment. Indeed, in this work, variations in the intensity  $S(\Delta_i)$  due to the finer structure in the PSB are taken into account through the variance  $\sigma$ . Capturing these fine details in the PSB is crucial to construct accurate models of the electron phonon coupling dynamics. Indeed, large variations in the spectral density caused by spectrally sharp phonon modes can induce non-trivial phonon-electron-photon correlations [23].

The full potential of our new approach, combining *ab initio* calculations with the polaron method, comes into light when compared to PLE measurements of our group I centers. In contrast to the generating function approach, our polaron model allows introducing an external driving field and thereby enables us to calculate theoretical PLE maps. By focusing on the most likely defect candidates and adding acoustic phonons to the spectral density, we found excellent agreement of the experimental PLE of one group I centre with  $C_2C_B$  and  $C_2C_N$  while we could exclude 24 other defect transitions. Our excellent agreement of experimental PLE with *ab initio* calculations is outstanding compared to previous work [33].

In our PLE experiments, we observed enhanced ZPL and PSB emission at one- and two-phonon detunings, the latter for the first time to the best of our knowledge. By resolving first- and second-order phonon transitions,

we confirmed indications of a phonon-assisted excitation mechanism with a phonon energy around 170 meV. In particular, it is very unlikely that other electronic states are equally-spaced by 170 meV for both ground and excited states. Moreover, such additional electronic states are not predicted by *ab initio* calculations for the most likely defect transitions. Our findings are supported by split first-order PSB of several group I centres as well as by a decent agreement of our excitation mechanism with *ab initio* calculations of  $C_2C_B$ . The methodology of combining PLE measurements and the polaron method with input from *ab initio* methods can be applied to identify the microscopic origin of other luminescent centres or single-photon emitters in hBN and other materials.

We are convinced that the presented comparison of experimental PLE maps with advanced models, able to combine atomistic calculations with open quantum system theory, provides the most accurate description of 2 eV luminescent centres in hBN and their excitation mechanism. For luminescent centres showing excellent agreement with  $C_2C_B$  and  $C_2C_N$ , lifetime measurements can give further insight since the theoretical values differ significantly [9]. To prove the quantum nature of the studied luminescent centres, auto-correlation ( $g^{(2)}$  function) and cross-correlation measurements [19] as well as polarisation-dependent measurements [39, 43] are required. Furthermore, bleaching [21, 30] and blinking [7, 41, 44] of 2 eV luminescent centres are unresolved challenges since only few centres were stable over minutes [2, 7, 19, 40, 45] or even months [29]. All in all, further experimental and theoretical work is needed to both unambiguously identify the nature of group I centres and to make 2 eV luminescent centres in hBN feasible for applications in quantum technologies.

As a last observation, we would like to point out that the ubiquitously used 532 nm laser efficiently excites luminescent centres with ZPL energies around 2.15 eV because the laser energy of 2.33 eV matches the one-phonon detuning of around 170 meV. This fortunate coincidence of the energy of an ubiquitously used laser with the one-phonon detuning has been a gift for the research field and explains why the majority of works on hBN report 2 eV luminescent centres.

## METHODS

### Scatter plot

The mean and variance shown in Fig. 1c and Supplementary Information IV are calculated for ZPL detunings from  $-440$  to  $10$  meV. We note that the only fitting parameter is the ZPL line width while the phonon broadening is kept constant (see Supplementary Information III).

The scatter plots reflect the agreement of the partial Huang-Rhys factors of each defect transition with the experimental line shape. The discussed scatter plots are similar to a recent theoretical study [12] focusing on the



combined defect and PSB emission spectrum (i.e. accessing the vibrational fine structure).

We note that in our scatter plots we focus on the mean and variance while higher-order variances need to be considered for perfect agreement between theory and experiment.

### *Ab initio* calculations

All the *ab initio* calculations for the ground states, excited states and normal modes were performed within the GPAW electronic structure code [46] using a plane-wave basis set with 800 eV plane wave cut-off and a  $\Gamma$ -point sampling of the Brillouin zone. All the defects were represented in a 7x7x1 supercell (monolayer) and allowed to fully relax until the maximum force was below 0.01 eV/Å. A vacuum of 15 Å was used in the vertical direction.

The PBE exchange correlation (xc-)functional [47] was used for all calculations. In addition, for  $C_2C_B$ ,  $C_2C_N$ , and  $V_NC_B$  the relatively more accurate HSE06 functional was used for the calculation of the ZPL energies. The excited states were calculated using the direct optimisation-maximum overlap matrix (DO-MOM) method [48] with a maximum step length,  $\rho_{\max}$ , for the quasi-Newton search direction of 0.2. Compared to the standard  $\Delta$ -SCF approach, the DO-MOM method yields improved convergence and avoids variational collapses during the SCF optimisation [48]. We highlight that the  $C_2C_N$  described here is the transition studied in Ref. [9]. For further details on the theory and calculation details we refer to our previous work [49].

In all calculations, we considered in-plane defect structures and verified their dynamical stability by the absence of imaginary frequencies in the  $\Gamma$ -point phonon spectrum. Only for the excited state of  $V_NC_B$ , i.e.  $(2)^3B_1$ , does the carbon atom of the defect relax out of plane. The out-of-plane configuration is stable compared to the planar configuration by 0.23 eV for monolayer hBN. This energy difference is only 0.036 eV in a trilayer hBN with a  $V_NC_B$  defect embedded in the central hBN layer (of the trilayer hBN) [7].

### Optical spectroscopy

The optical characterisation is described in detail in Supplementary Information XI. For PLE measurements at low temperature, we used a supercontinuum white light laser in combination with a tunable laser line filter resulting in a PLE resolution of  $\sim 5$  meV.

### Open quantum system

To model experimental PLE maps we use information about the phonon modes extracted from the *ab initio* calculations to construct an open system model for the defect transition. The emitter is modelled as a two level system with ground and excited states  $|g\rangle$  and  $|e\rangle$  respectively, with transition energy  $\hbar\omega_e$ . The emitter is driven by a continuous-wave laser with angular frequency  $\omega_L$ , and interacts both with vibrational and electromagnetic environments. The form of this interaction is given in the Supplementary Information XII. To account for strong electron-phonon coupling and resultant PSB observed for luminescence centres, we make use of the po-

laron method [18, 50]. This approach dresses the system energy levels with modes of the vibrational environment using a unitary transformation, providing an optimised basis in which to do perturbation theory. We then derive a Born-Markov master equation in the transformed frame which is non-perturbative in the original electron phonon interactions. This allows us to describe the dynamics [50] and, crucially, the PSB of the optical transition in question [24, 25]. For further details of the model described above, we refer the reader to the Supplementary Information III and XII.

We note that the expression of  $J_{\text{acoustic}}(\omega)$  uses a different definition of the spectral density compared to Ref. [18] which can be obtained by multiplying  $J_{\text{acoustic}}$  with  $\omega^2$  and  $\alpha$  with  $\omega_c^{-2}$ . The physical description remains unchanged, i.e. in both cases a three-dimensional acoustic phonon environment is used.

### Excitation mechanism

In Fig. 3a, the band gap is given by  $E_g \sim 6$  eV [36] and the Fermi level is  $E_F$ . Within the empiric mechanism, the two relaxation processes  $\Delta_e$  and  $\Delta_g$  are associated with  $|e\rangle$  and  $|g\rangle$ , respectively. In the phonon-assisted and advanced excitation mechanisms, we do not show the Fermi level for clarity. Furthermore, the excited states are labelled with  $|e, n\rangle$  corresponding to the electron in the excited state and its environment occupied by  $n$  phonons. Similarly,  $|g, m\rangle$  describes the electron in the ground state with  $m$  phonons in its environment.

### One- and two-phonon processes

To identify one- and two-phonon processes, we use the electronic states  $|e, n\rangle$  and  $|g, m\rangle$  of the phonon-assisted excitation mechanism presented in Fig. 3a.

At a laser detuning of  $\sim 170$  meV, we excite the electronic state  $|e, 1\rangle$  that relaxes to  $|e, 0\rangle$  by the emission of one phonon. From  $|e, 0\rangle$ , the ZPL emission is realised without any further phonon emission, while the PSB process involves another phonon that is emitted by the relaxation from  $|g, 1\rangle$  to  $|g, 0\rangle$ . Therefore, the ZPL is a one-phonon process while the PSB is a two-phonon process. The above described two-phonon process holds for both optical PSB at 160 and 190 meV as well as the acoustic PSB at  $\sim 10$  meV.

At laser detunings of  $\sim 340$  meV we excite the state  $|e, 2\rangle$ , introduced in the phonon-assisted mechanism in Fig. 3a. This state relaxes by the emission of two phonons to  $|e, 0\rangle$  from where a ZPL emission is realised without any further phonon emission. Thus, this process is also a two-phonon process like the optical PSB at  $\sim 170$  meV detuning.

### Acknowledgements

**Funding:** This work was funded by the Danish National Research Foundation through the Center for Nanostructured Graphene (project number DNRF103) and through NanoPhoton - Center for Nanophotonics (project number DNRF147). M.F. and N.S. ac-

knowledge support from the VILLUM FONDEN (project number 00028233). Parts of our optical setup are financed through the IDUN Center of Excellence founded by the Danish National Research Foundation (project number DNRF122) and VILLUM FONDEN (project number 9301). N.S. and M.W. acknowledge support from the Independent Research Fund Denmark, Natural Sciences (project number 0135-00403B). S.X. acknowledges support from the Independent Research Fund Denmark, Technology and Production Sciences (project number 9041-00333B) and Natural Sciences (project number 2032-00351B). D.I.M. and S.C. acknowledge support from the Independent Research Fund Denmark, Sapere Aude grant (project number 8049-00095B). S.A. and K.S.T. acknowledge funding from the European Research Council (ERC) under the European Union's Horizon 2020 research and innovation program Grant No. 773122 (LIMA) and the Novo Nordisk Foundation Challenge Programme 2021: Smart nanomaterials for applications in life-science, BIOMAG Grant NNF21OC0066526. K.S.T. is a Villum Investigator supported by VILLUM FONDEN (grant no. 37789). A.H., C.K., and A.W.H. gratefully acknowledge the German Science Foundation (DFG) for financial support via the clusters of excellence MCQST (EXS-2111) and e-conversion (EXS-2089), as well as the state of Bavaria via the One Munich Strategy and the Munich Quantum Valley, and TUM-IGSSE for

project BrightQuantTUM.

#### Author contributions

M.F. and A.H. carried out the experiments. M.F. and N.S. analysed and interpreted the experimental data. A.S. designed and performed the *ab initio* calculations. K.S.T. supervised the *ab initio* calculations. J.I.-S. developed the open quantum systems model, and fitted the theoretical curves to the experimental data. M.F., A.S., J.I.-S., A.H., K.S.T., A.W.H. and N.S. discussed the experimental results and compared them with the theoretical predictions. A.S. and J.I.-S. equally contributed to the theoretical part of this manuscript. All authors contributed to the writing of the manuscript.

#### Note

During the preparation of this manuscript we became aware about a thorough study of defects in hBN, focusing on tailoring the ZPL energy [51].

#### Competing interests

The authors declare that they have no competing interests.

SUPPLEMENTARY MATERIALS  
 COMBINING EXPERIMENTS ON LUMINESCENT CENTRES IN HEXAGONAL BORON NITRIDE  
 WITH THE POLARON MODEL AND AB INITIO METHODS TOWARDS THE IDENTIFICATION OF  
 THEIR MICROSCOPIC ORIGIN

I. FURTHER GROUP I SPECTRA

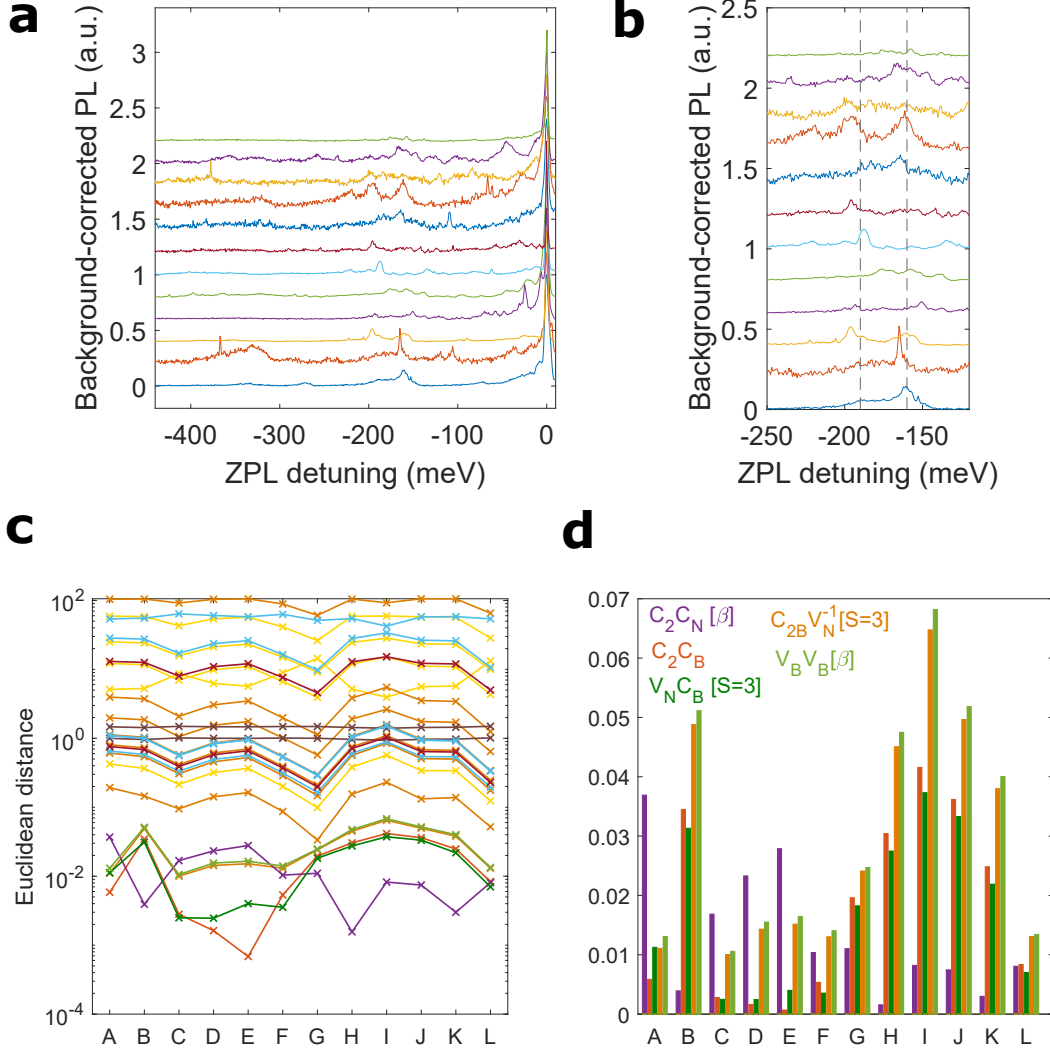


FIG. 4. **Low-temperature photoluminescence of luminescent centres belonging to group I.** (a) Photoluminescence line shapes at  $T = 10$  K under  $2.37$  eV excitation, shifted vertically for clarity. The spectra from bottom to top correspond to Emitter A to Emitter L, given by the x axis in (c). (b) Optical PSB of the luminescent centres shown in (a) with corresponding colors, shifted vertically for clarity. The vertical dashed lines are at detunings of  $160$  and  $190$  meV, respectively. (c) Euclidean distance for Emitter A up to Emitter L, with corresponding spectra shown in (a) from bottom to top. (d) Histograms of Emitter A to Emitter L. The colors correspond to the defect transitions given by the legend. All line shapes are background corrected as outlined in Supplementary Information V and more details are given in the main text.

A	B	C	D	E	F	G	H	I	J	K	L
2.1528	2.1785	2.0122	2.2500	2.1797	2.2045	2.2133	2.1652	2.2058	2.0819	2.1703	2.1984

TABLE II. Zero-phonon line energies (in electron-volt) of Emitter A to L.

## II. DETAILS ON *AB INITIO* CALCULATIONS

### Nomenclature of defect transitions

In the main text, we suppress the notations for the spin majority channel  $\alpha$  as well as non-triplet spin states. For  $C_2C_B$ , this results in

$$C_2C_B[S = 2, \alpha] \equiv C_2C_B, \quad (2)$$

where  $\equiv$  stands for an equal representation. Another example is  $C_2C_N[S = 2, \beta] \equiv C_2C_N[\beta]$ .

Defect	Charge and spin state	$\alpha$			$\beta$		
		ZPL(eV)	$\Delta Q$	HR	ZPL(eV)	$\Delta Q$	HR
$C_2C_N - V_N$	$C_2C_N - V_N$ [S=3](E=2.15eV)	0.2	1.3	7.45	0.96	1.76	19.7
	$C_2C_N - V_N$ [S=0](E=0.0eV)	1.96	0.8	5.72	-	-	-
	$C_2C_N - V_N^{+1}$ [S=2]	-	-	-	0.72	1.42	15.7
	$C_2C_N - V_N^{-1}$ [S=2]	-	-	-	1.96	1.3	9.1
$C_2NV_N$	$C_2NV_N$ [S=2]	2.08	1.083	7.16	-	-	-
	$C_2NV_N^{+1}$ [S=0](E=0.0eV)	2.2	0.83	4.14	-	-	-
	$C_2NV_N^{-1}$ [S=3](E=1.43eV)	1.7	0.72	3.82	1.07	0.411	2.9
	$C_2NV_N^{-1}$ [S=0](E=0.0eV)	1.47	1.31	9.05	-	-	-
$C_2BV_N$	$C_2BV_N$ [S=2]	1.41	1.08	5.67	1.1	0.8	5.07
	$C_2BV_N^{-1}$ [S=0]	0.77	0.61	3.2	-	-	-
	$C_2BV_N^{-1}$ [S=3](E=0.64eV)	0.9	0.29	0.635	1.17	0.8	4.99
	$C_2BV_N^{+1}$ [S=0](E=0.0eV)	0.7	0.9	5.56	-	-	-
$C_2CB - V_B$	$C_2CB - V_B$ [S=3](E=0.0eV)	1.39	3.05	45	-	-	-
	$C_2CB - V_B^{-1}$ [S=2]	0.74	13.52	36.8	-	-	-
$V_BV_B$	$V_BV_B$ [S=3]	-	-	-	2.7	0.41	0.3
$C_B C_N V_N$	$C_B C_N V_N^{+1}$ [S=3](E=3.92eV)	1.37	0.92	10.5	-	-	-
	$C_B C_N V_N^{+1}$ [S=0](E=0.0eV)	2.95	1.19	7.45	-	-	-
$C_2C_N$	$C_2C_N$ [S=2]	-	-	-	1.51	0.25	1.2
$C_2C_B$	$C_2C_B$ [S=2]	1.16	0.24	1.1	-	-	-
$V_N C_B$	$V_N C_B$ [S=3]	1.39	0.53	1.58	-	-	-
$C_2C_N$ , HSE06	$C_2C_N$ [S=2]	-	-	-	1.67	0.261	1.26
$C_2C_B$ , HSE06	$C_2C_B$ [S=2]	1.36	0.26	1.2	-	-	-
$V_N C_B$ , HSE06	$V_N C_B$ [S=3]	1.75	0.53	1.50	-	-	-

TABLE III. **Zero-phonon lines (ZPL), momentum displacements ( $\Delta Q$ ) and Huang-Rhys factors (HR) of all studied defects.** Here,  $\alpha$  refers to the majority spin channel and  $\beta$  to the minority spin channel. The energy  $E$  in the second column gives the energy difference between the singlet and triplet states. It is only given for defects that show both a singlet and a triplet state. The PBE functional is used for all calculations except for the last three rows where the HSE06 functional was used.

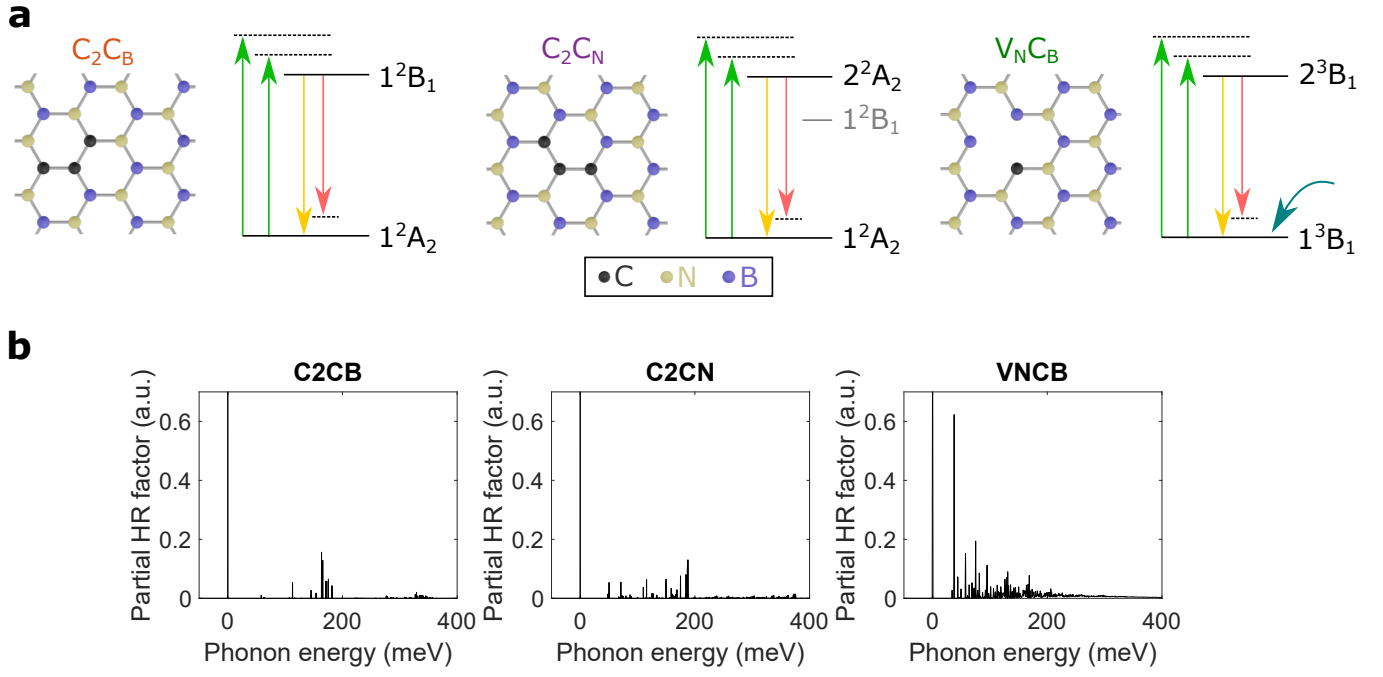


FIG. 5. **Schematics, electronic levels and partial Huang-Rhys factors for  $C_2C_B$ ,  $C_2C_N[\beta]$ , and  $V_N C_B[S = 3]$ .** (a) Schematics and electronic levels of  $C_2C_B$ ,  $C_2C_N[\beta]$ , and  $V_N C_B[S = 3]$  where the latter is taken from Ref. [22]. (b) The partial Huang-Rhys factors for  $C_2C_B$ ,  $C_2C_N[\beta]$ , and  $V_N C_B[S = 3]$  are shown from left to right. We highlight that the HSE06 functional was used for all three defects.

### III. FITTING AND COMPARISON WITH EXPERIMENT

In this section we outline the fitting procedure used to compare the polaron method to experiment. The fitting is done in two parts, in the first we extract the width of ZPL, the second fits the inhomogeneous broadening about the ZPL associated to acoustic phonons. To do both of these fits, we consider the emission lineshape driven by an excitation laser with detuning  $\hat{\Delta} = 168$  meV. We also assume that the phonons decay on a much faster timescale than light emission occurs, which allows us to ignore the excitation effects during the fitting procedure. This allows us to disregard the coherent driving term  $\Omega_R \sigma_x / 2$  and the phonon dissipator  $\mathcal{K}_{\text{PH}}$  in Eq. 11, and assume that the emitter is initially in its excited state.

#### A. Fitting the zero-phonon line

To fit the ZPL, we restrict the experimental data to a frequency window  $\pm 0.008$  eV around the measured ZPL. This allows us to ignore the phonon sideband contribution, fitting only the ZPL with only function  $S_{\text{opt}}(\omega)$ . For an emitter initially in its excited state, the ZPL spectrum reduces to a simple Lorentzian lineshape:

$$S_{\text{opt}}(\Delta\omega) \approx \frac{B^2}{2\Gamma} \frac{\Gamma + \gamma}{(\Gamma + \gamma)^2 + \Delta\omega^2}, \quad (3)$$

where  $\Delta\omega$  is the detuning from the emitter frequency. After first normalising the data and the above expression to the peak of the ZPL, we do a least min-squared fit. Note that we can fit only a single rate, since  $\Gamma$  and  $\gamma$  combine to give a single width of the Lorentzian, thus we set  $\gamma = 0$  without loss of generality. We find an optimal  $\Gamma = 3.15$  meV with residual of  $r = 0.098$  for Emitter A.

#### B. Describing electron-phonon sidebands in photoluminescence

As discussed in the main tex, we divide the phonon spectral density into two components  $J_{\text{Ph}}(\omega) = J_{\text{FP}}(\omega) + J_{\text{A}}(\omega)$ . The first contribution,  $J_{\text{FP}}(\omega) = \sum_{\mathbf{k}} S_{\mathbf{k}} \delta(\omega - \omega_{\mathbf{k}})$ , captures the phonons calculated from first principles, where  $S_{\mathbf{k}}$  is the partial Huang-Rhys factor associated with a phonon with frequency  $\omega_{\mathbf{k}}$  [23]. To move to a continuum limit version, we account for the natural lifetime of phonons in a material by approximating the  $\delta$ -functions in the definition of  $\mathcal{J}_{\text{Ph}}(\nu)$  with a Gaussian function  $\delta(\omega) \approx [\sigma\sqrt{2\pi}]^{-1} \exp[-(\omega/\sqrt{2}\sigma)^2]$ , where  $\sigma$  is the phonon broadening parameter. We choose the broadening parameter as  $\sigma = 5$  meV, such that it phenomenologically reproduces features in the emission spectrum at low temperature.

The second contribution to the phonon spectral density,  $J_{\text{A}}(\omega)$ , is associated to acoustic phonons, and leads to the inhomogeneous broadening around the ZPL, which is not captured by the first-principle calculations. We assume that this spectral density takes the form  $J_{\text{A}}(\omega) = \alpha\omega_c^{-2}\omega e^{-\omega^2/\omega_c^2}$  [18], where  $\alpha$  and  $\omega_c$  are left as fitting parameters. This form of spectral density is commonly used in the semiconductor quantum dot literature, where it describes bulk acoustic phonons. Similarly to the ZPL fits we restrict ourselves to a frequency window of  $-0.06$  eV  $< \Delta\omega < 0.01$  eV. In contrast to the ZPL fits, however, we use the full expression for the emission spectrum, including the full phonon sideband given in Section XII C. The value of the optimal phonon parameters extracted from these fits changes depending on the defect. It was not possible to obtain a fit for the acoustic phonon sideband for  $V_{\text{N}}C_{\text{B}}$  due to the discrepancy between the sideband produced by first principles calculations and the measured PL. For illustrative reasons, we use the acoustic phonon parameters associated to  $C_2C_{\text{N}}$  when plotting the theoretical  $V_{\text{N}}C_{\text{B}}$  PL.

Fig. 6 shows the fitted PL lineshapes for the three defects considered in the manuscript. We compare the cases where acoustic phonons are neglected (dashed) and included (solid). For the  $C_2C_{\text{N}}$  and  $C_2C_{\text{B}}$  defect complexes, we see improved agreement about the ZPL when acoustic phonons are included.  $V_{\text{N}}C_{\text{B}}$  remains a are poor fit, with and without acoustic phonons. Notably, when acoustic phonons are included, we observe additional acoustic sidebands on the phonon replicas found from DFT calculations.

#### C. Theoretical photoluminescence emission spectroscopy

The model presented above, and the resulting fits, allow us to calculate the PLE directly from the full phonon model. We do this by varying the detuning of the continuous wave driving laser,  $\Delta$ , and calculating the emission

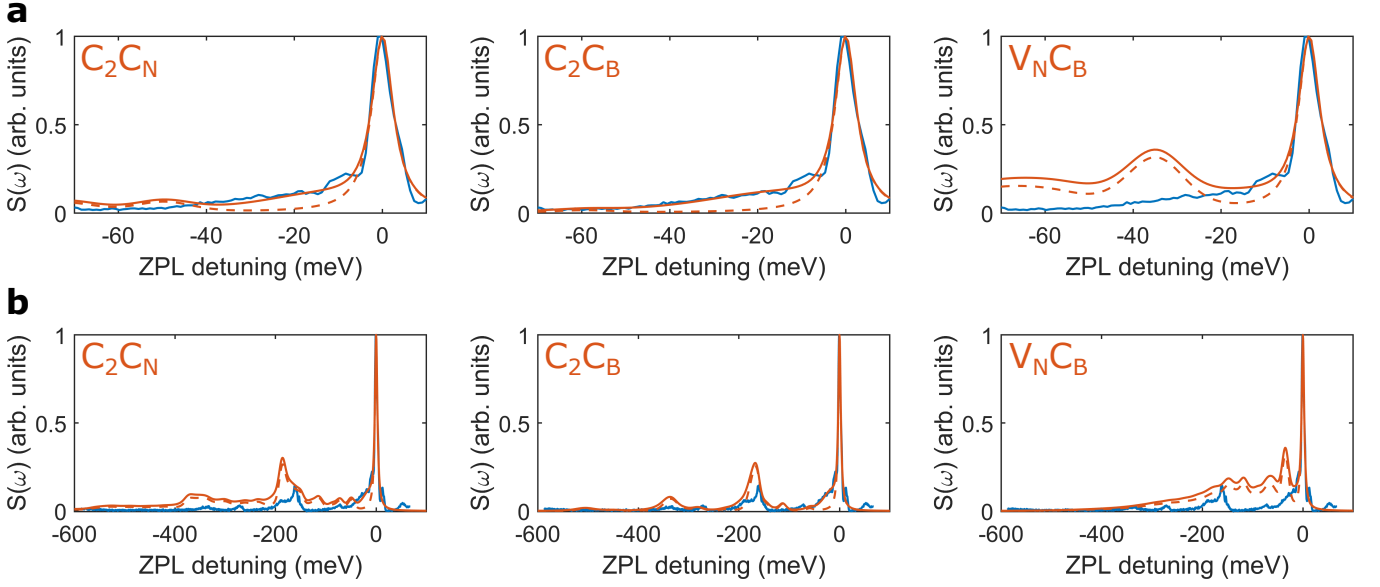


FIG. 6. Comparison of the experiment (blue) and theory fits for three main defects considered in the main text. The dashed curves include only phonons calculated through *ab initio* calculations, while the solid orange curves show the fits with acoustic phonons. The spectra plotted in (b,d,f) are the same as (a,c,e) respectively, plotted over a larger range. Temperature is set to  $T = 10$  K.

spectrum for each detuning. For the driven case, we consider the steady-state emission spectrum, defined as:

$$S(\omega) = \text{Re} \left[ \lim_{t \rightarrow \infty} \int_0^{\infty} d\tau \mathcal{G}(\tau) g_{\text{opt}}^{(1)}(t, \tau) \right], \quad (4)$$

where the integral over  $t$  has been reduced to the steady state limit.

Fig. 7 shows the PLE for the three defects considered in the main manuscript.

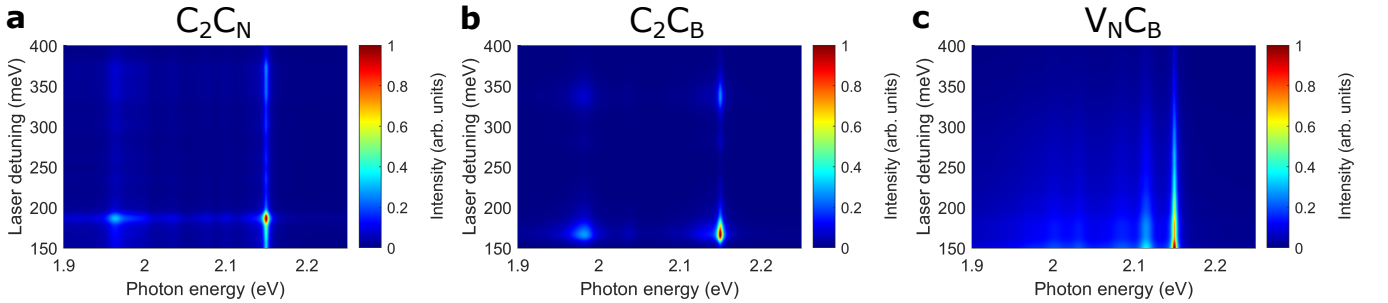


FIG. 7. Theoretical PLE maps fitted to Emitter A. The calculated PLE maps include electron-phonon interactions as described in the main text.

Fig. 8 shows the photoluminescence for  $C_{2B}V_N^{-1}[S=3]$  which does not conform nicely with the experiment.

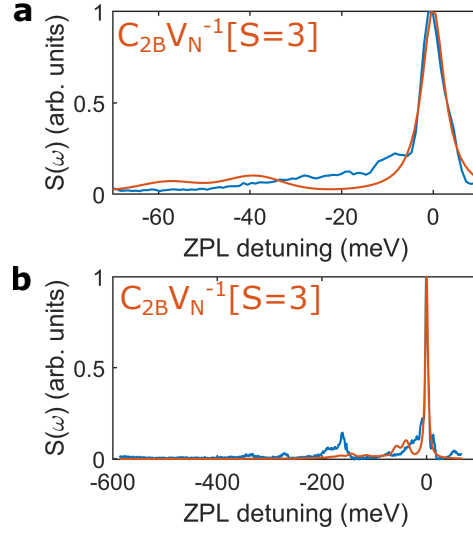


FIG. 8. Comparison of the experimental photoluminescence (blue) with the theoretical spectrum of  $C_{2B}V_N^{-1}[S=3]$  (red). The theoretical spectrum is calculated without acoustic phonons. The spectra in (a) and (b) are identical but plotted over different ranges.



## IV. DETAILED SCATTER PLOTS

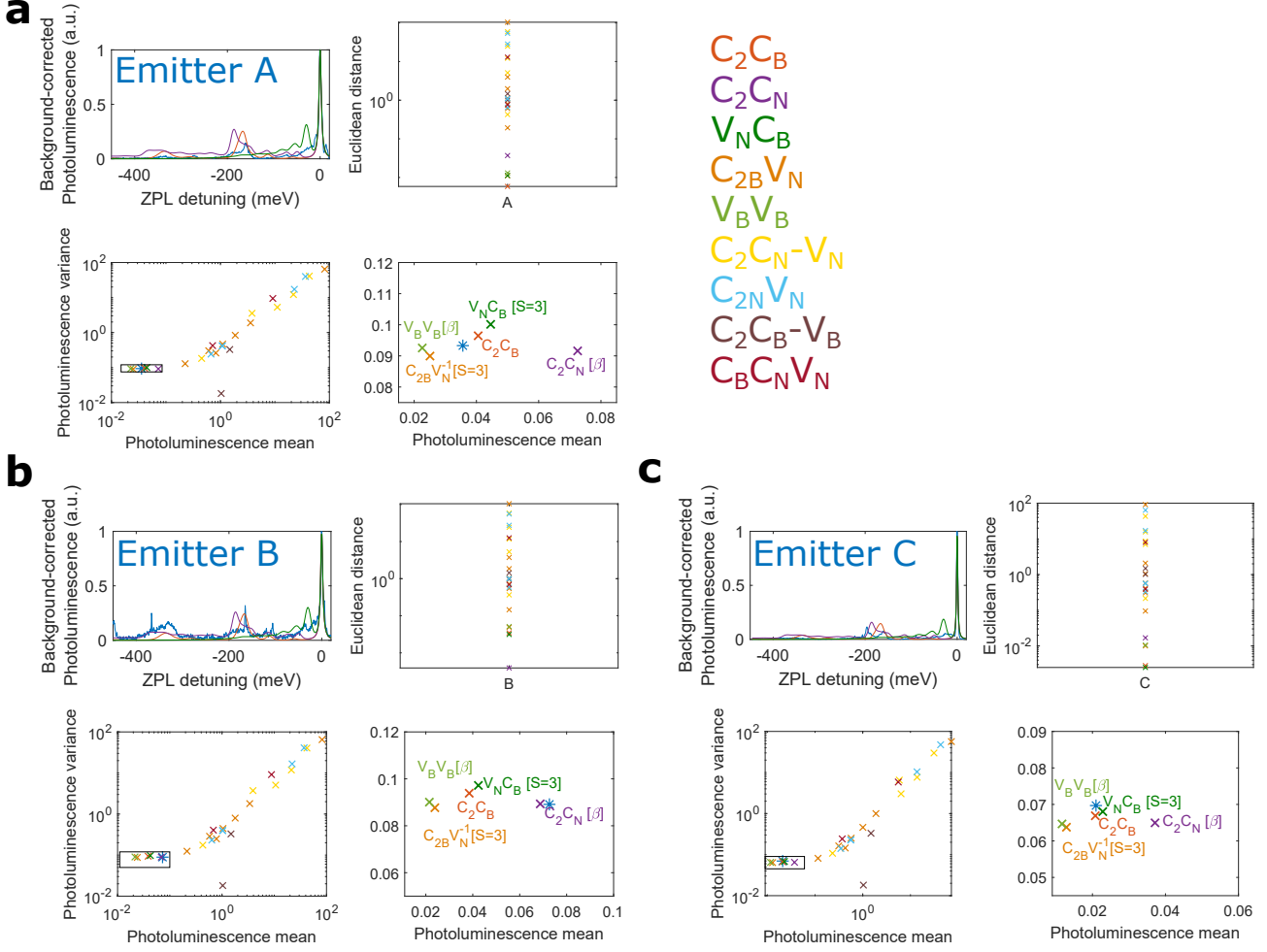


FIG. 9. **Detailed scatter plot for all studied defects.** (a) Emitter A. The top left panel shows the experimental photoluminescence as well as the theoretical line shapes of  $C_2C_B[\beta]$  (red),  $C_2C_N$  (purple), and  $V_N C_N[S=3]$  (dark green). The bottom panels show the scatter plot with a zoom-in on the right side, indicated by a square in the left plot. The top right panel shows the euclidean distance. The colors of the defects are given on the right. (b) Emitter B, labelling as in (a). (c) Emitter C, labelling as in (a).

## V. BACKGROUND CORRECTION AND FURTHER LOW-TEMPERATURE PSB

For easy comparison of PSB, we carried out a background correction via a publicly available script [52]. We use this script with the asymmetric Huber function at fourth order and  $s = 0$ . In Fig. 10, we show the background correction for one photoluminescence spectrum.

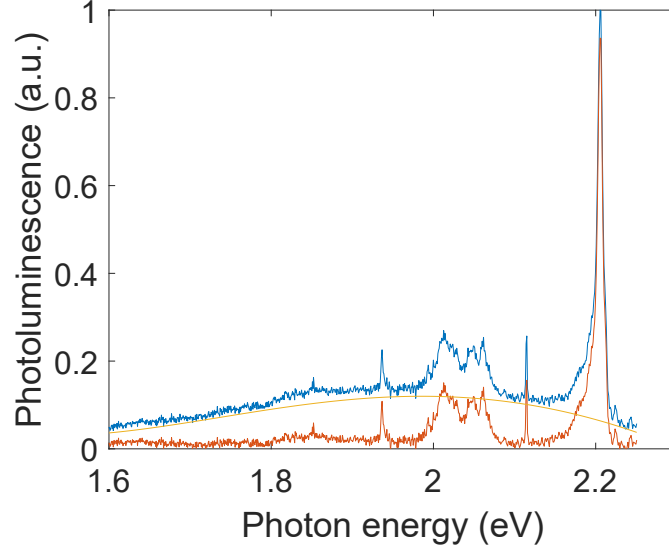


FIG. 10. **Background correction of photoluminescence line shapes.** Background correction of one photoluminescence spectrum. The raw spectrum is shown in blue, the background in yellow and the background-corrected spectrum in red.

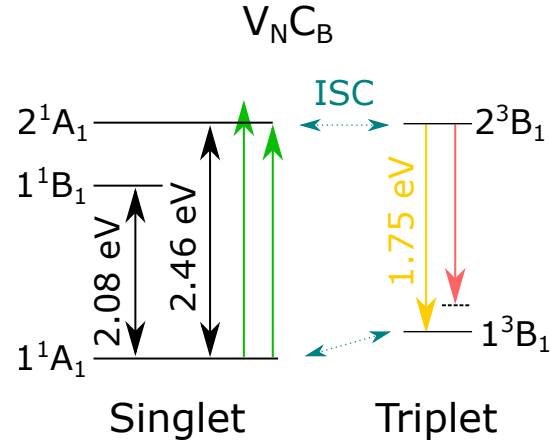
VI. EXTENDED LEVEL MECHANISM OF  $V_N C_B$ 

FIG. 11. **Extended level mechanism of  $V_N C_B$ .** The singlet system is shown on the left and the triplet system on the right. Emission from the triplet state is not possible by direct excitation because the ground state of the triplet state is not populated in equilibrium. However, optical excitation of the singlet system followed by an intersystem crossing (ISC) is possible. This requires laser detunings that are higher than  $2.46 - 1.75 \text{ eV} = 0.71 \text{ eV}$ . This is significantly larger than our experimental laser detunings from  $\sim 150$  to  $400 \text{ meV}$ .

## VII. FURTHER EXPERIMENTAL PLE DATA

Fig. 12 and 13 show the PLE data for Emitter A, B and C without any background correction, i.e. both photoluminescence and PLE intensities are shown without background correction.

Fig. 12a shows the photoluminescence spectra for several laser detunings. We obtain strong variations with laser detuning that are investigated in detail under continuous laser detuning, as shown in Fig. 12c. To investigate the absorption characteristic, we study the ZPL intensity which is defined as the area under the ZPL with a bandwidth of 10 meV (Fig. 12b). We observe a strong ZPL intensity at a detuning of 168 meV while an intermediate ZPL intensity is obtained at a detuning of 341 meV. These two important detunings are highlighted by horizontal lines in Fig. 12c and the corresponding photoluminescence spectra are shown in Fig. 12a. Another important detuning is exactly between the two aforementioned, i.e. at 255 meV, which yields a small ZPL intensity because it lays between the two states  $|e, 1\rangle$  and  $|e, 2\rangle$ .

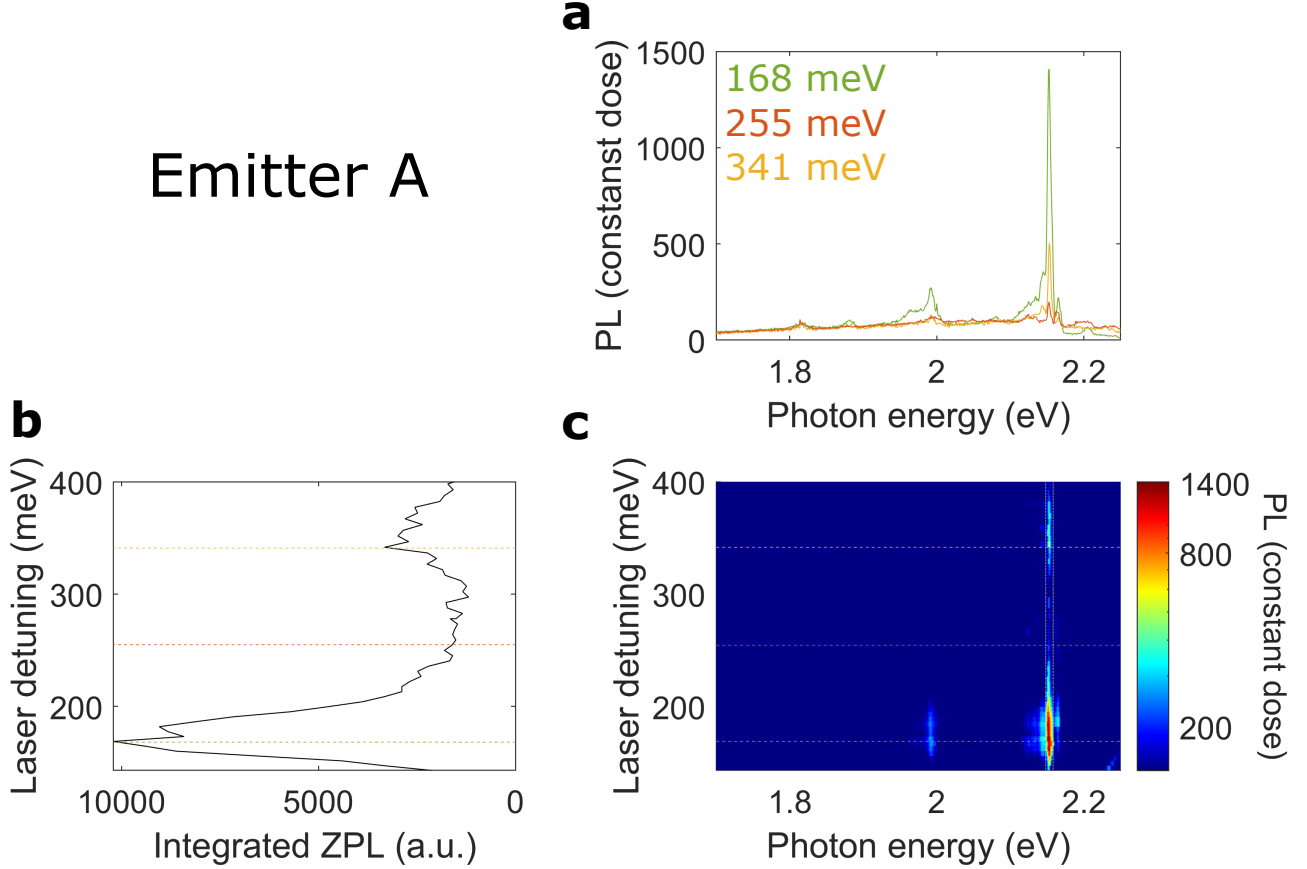


FIG. 12. **PLE of Emitter A at 10 K.** (a) Photoluminescence spectra of the luminescent centre at several laser detunings, given by the legend. (b) ZPL intensity as a function of laser detuning. The spectral range for the ZPL intensity is shown by the vertical lines in (c). (c) PLE map of a luminescent centre in hBN. The horizontal lines correspond to the spectra shown in (b) and the dim upward line in the bottom right corner corresponds to the silicon Raman  $\sim 520 \text{ cm}^{-1}$ .

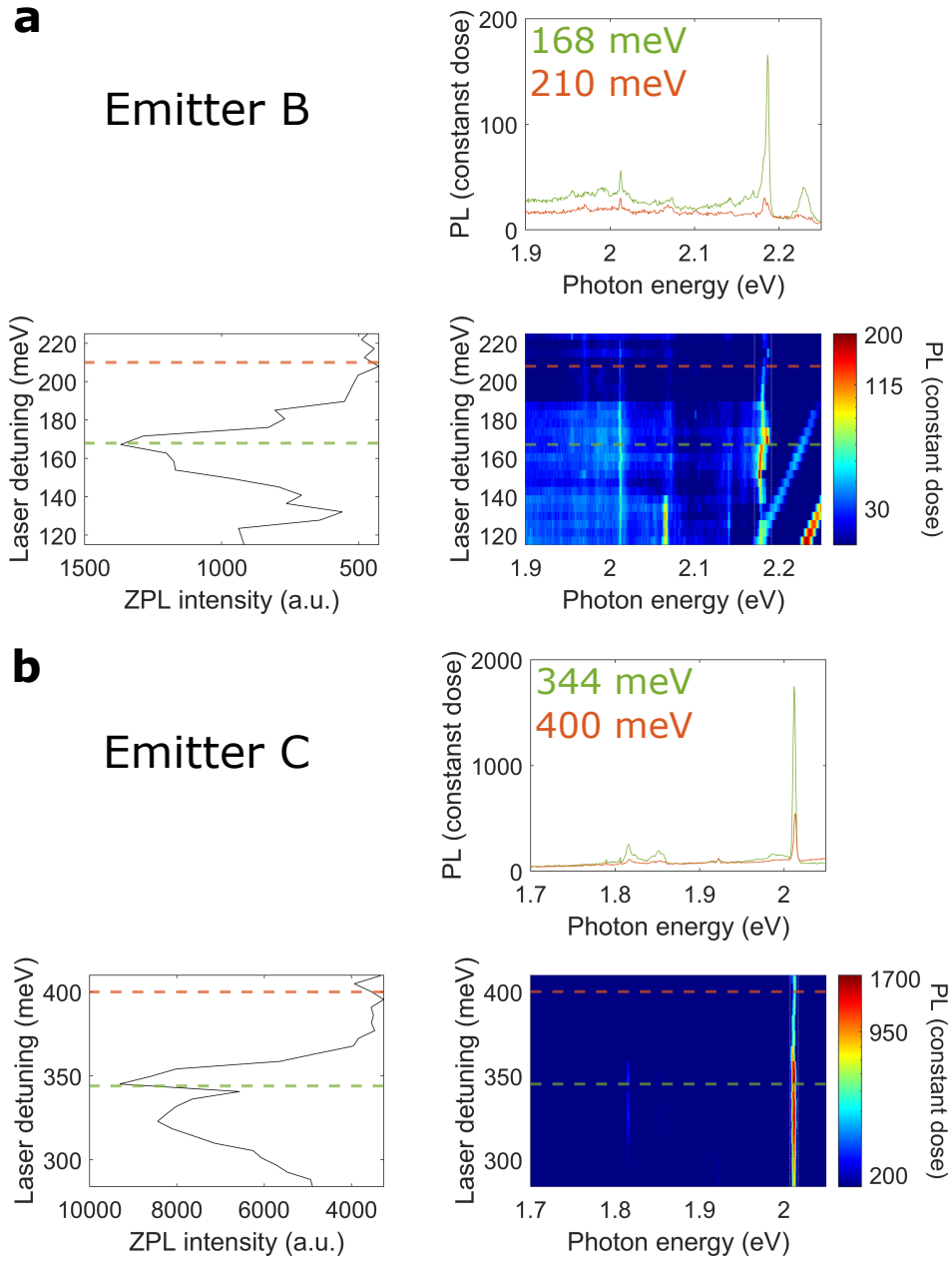


FIG. 13. **PLE of further luminescent centres at 10 K.** (a) PLE measurement of Emitter B, arranged and labelled as in Fig. 12. (b) PLE measurement of Emitter C, arranged and labelled as in Fig. 12.

### VIII. RESCALING OF PLE SPECTRA FOR EMITTER A

The PLE measurements shown in Fig. 2a are done by two laser sweeps: Sweep 1 and Sweep 2. We use two different laser settings to keep the power between 0.75 and 1.93 mW (see Fig. 14a). We first describe the rescaling within one sweep, followed by the rescaling between two sweeps. We finally describe the rescaling to one excitation power.

We measure the excitation power as a function of excitation energy prior to the PLE measurements (Fig. 14a). Within one sweep, the exposure time at power  $P_i$  is set to

$$t_1 \cdot \frac{P_1}{P_i}, \quad (5)$$

where  $t_1$  and  $P_1$  are the exposure time and power at the beginning of the sweep while  $P_i$  is the current power (at a specific laser energy or laser detuning). This adjustment in exposure time is meaningful, since the luminescent centres studied show a linear dependence of the intensity with excitation power in the studied power range, as shown in Fig. 14d. Furthermore, the detector operates in a constant-count regime which avoids saturation.

At each laser detuning in Sweep 2, the exposure time is adjusted as described by equation (5). To rescale the spectra of Sweep 2 to Sweep 1, we multiply each spectrum of Sweep 2 (after adjusting the exposure time) by

$$\frac{t_1}{t_1^*} \cdot \frac{P_1}{P_1^*}, \quad (6)$$

where  $t_1^*$  and  $P_1^*$  are the exposure time and the excitation power at the beginning of Sweep 2.

We will give an example why this multiplication is meaningful. At the end of Sweep 2, the excitation energy is identical to the beginning of Sweep 1. However, the excitation power at the end of Sweep 2 is  $P_{\text{end}}^*$ . Now we calculate the exposure time at the end of Sweep 2. Calculating the exposure time of Sweep 2, we multiply equation (5) with equation (6) and get

$$t_1^* \cdot \frac{P_1^*}{P_{\text{end}}^*} \cdot \frac{t_1}{t_1^*} \cdot \frac{P_1}{P_1^*} = t_1 \cdot \frac{P_1}{P_{\text{end}}^*} \quad (7)$$

which is identical to the exposure time given by equation (5) where  $P_i$  is replaced by  $P_{\text{end}}^*$ .

After carrying out all the rescaling mentioned above, we rescale the data to 1 mW at an excitation energy of 2.431 eV. This is the reason why we have shown absolute values in the photoluminescence (i.e. constant dose) in Fig. 2.

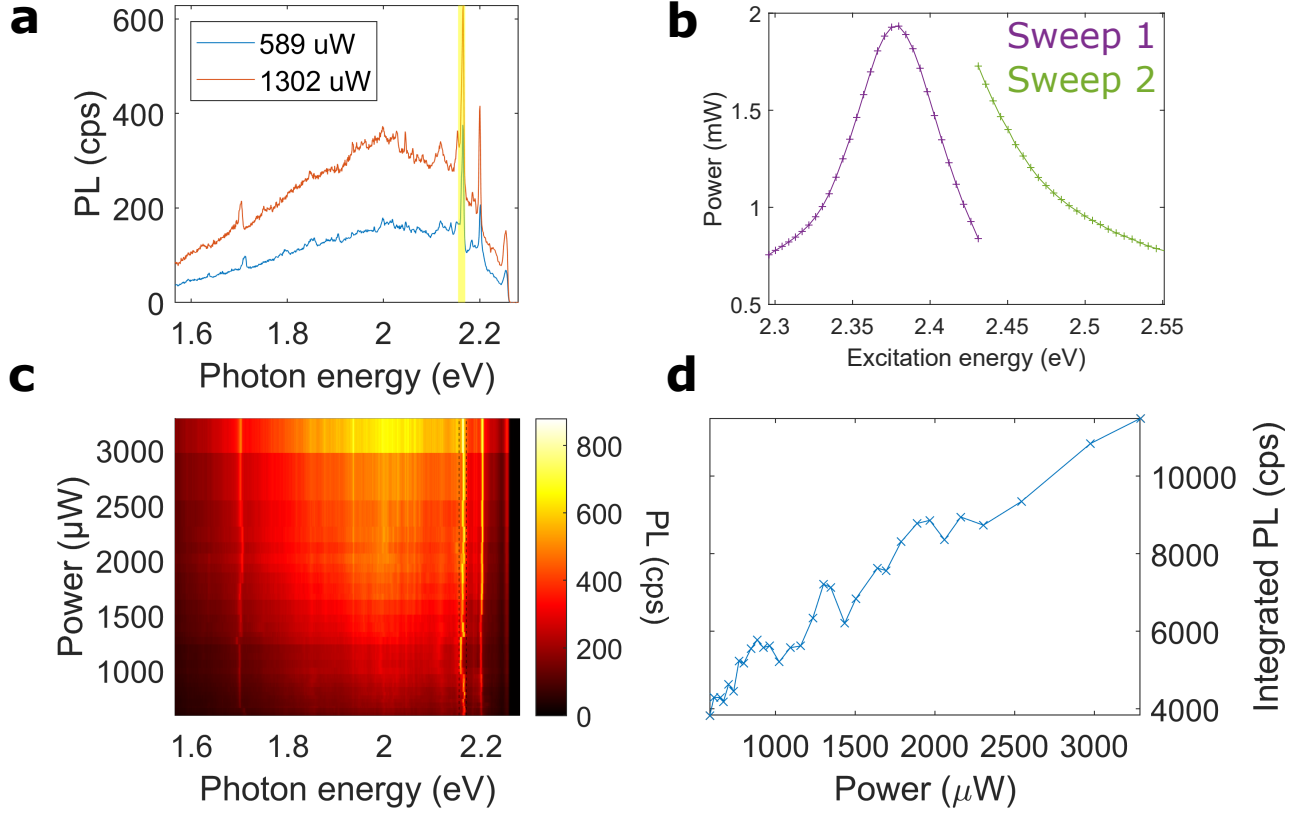


FIG. 14. **Power dependence of excitation source and photoluminescence.** (a) Photoluminescence spectra at several excitation powers, given by the legend. (b) The excitation power as a function of excitation energy. We performed two laser sweeps with different laser settings to obtain a similar power for all laser detunings. (c) Power-dependent photoluminescence, cps, counts per second. (d) Integrated zero-phonon line (ZPL) as a function of excitation power (not background corrected). The integrated spectral range (2.155 to 2.170 eV) is shown by vertical dashed lines in (c). We observe a linear dependence of the ZPL intensity as a function of excitation power.

## IX. PLE OF OPTICAL AND ACOUSTIC PSB OF EMITTER A

Fig. 15a shows how background-corrected PLE intensities are obtained, by using the ZPL intensity as an example. We use an unrelated photoluminescence range with the same width as the ZPL to define a background intensity (grey curve in the central panel). To obtain the background-corrected ZPL intensity, we subtract this background intensity. The resulting background-corrected ZPL intensity is shown in the right panel of Fig. 15a. Similarly, we obtain the background-corrected intensities for several PSB, as shown in Fig. 15b and in the main text.

Fig. 15b shows the optical PSB intensities. The right panel shows that the optical PSB intensities at one-phonon detuning (170 meV) and the ZPL intensity at two-phonon detuning (340 meV) show comparable strength. All these processes are two-phonon processes (see Methods of the main text).

Fig. 15c shows the low-energy PSB at detunings around 10 meV. The low-energy PSB intensity is lower than for the ZPL, since it is a two-phonon process (see Methods and discussion in the main text). For the background-corrected intensities, we observe an almost identical qualitative behaviour of the low-energy PSB and ZPL intensity. This supports our interpretation that the low-energy PSB and the ZPL have the same excitation mechanism.

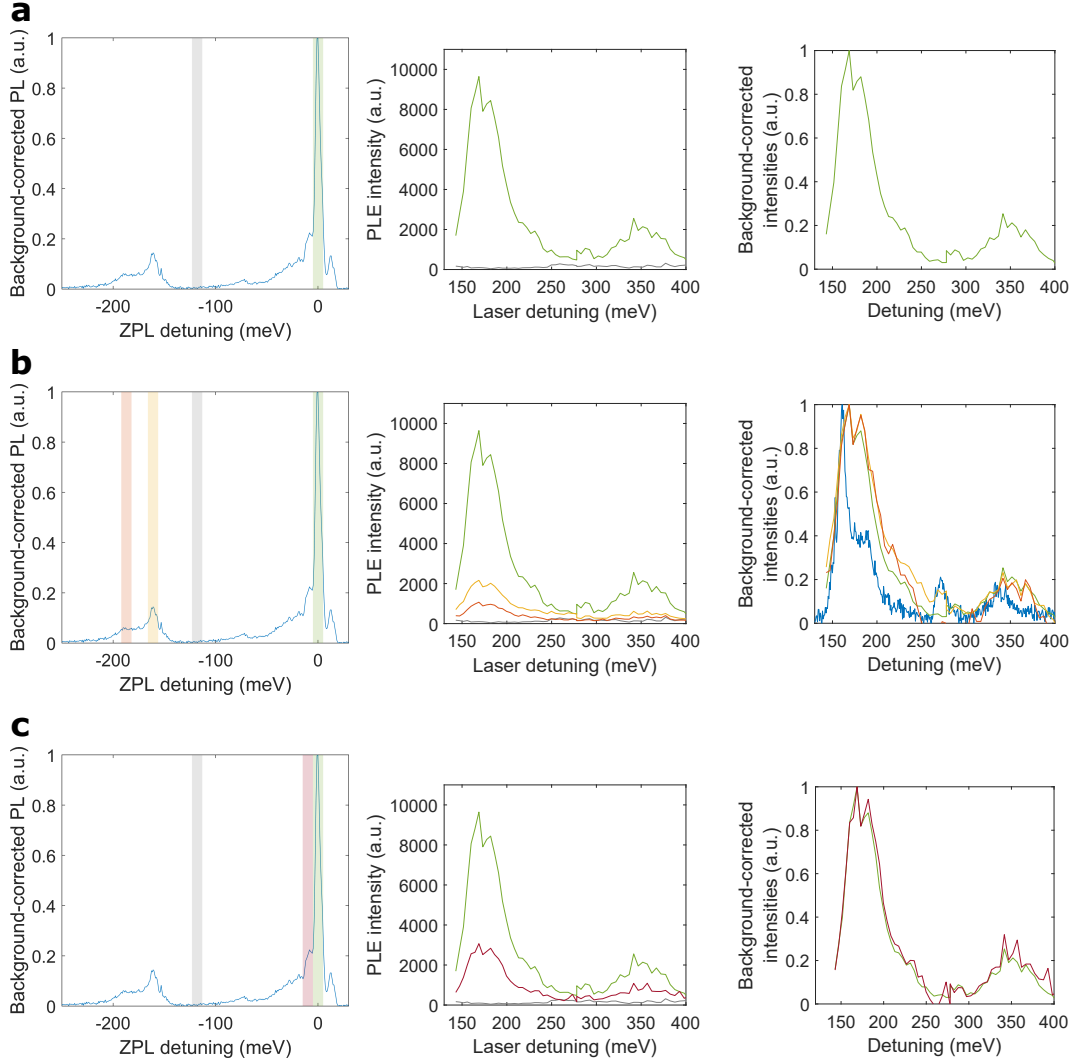


FIG. 15. **Background-correction of PLE intensities and acoustic PSB.** (a) Background-correction of the ZPL intensity. The spectral ranges of ZPL and background are shown in the left panel, on top of the photoluminescence spectrum. The resulting PLE intensities are shown in the central panel and the background-corrected ZPL intensity in the right panel. The latter is defined as the green ZPL intensity minus the grey background intensity. The photoluminescence spectrum in (a) is taken at a detuning of 168 meV. (b) Optical PSB intensities, labelled as in (a). In the right panel, the flipped photoluminescence spectrum is shown in blue. (c) Low-energy PSB intensity, labelling as in (a).



### X. EXPERIMENTAL LINE SHAPES DIFFERENT TO GROUP I

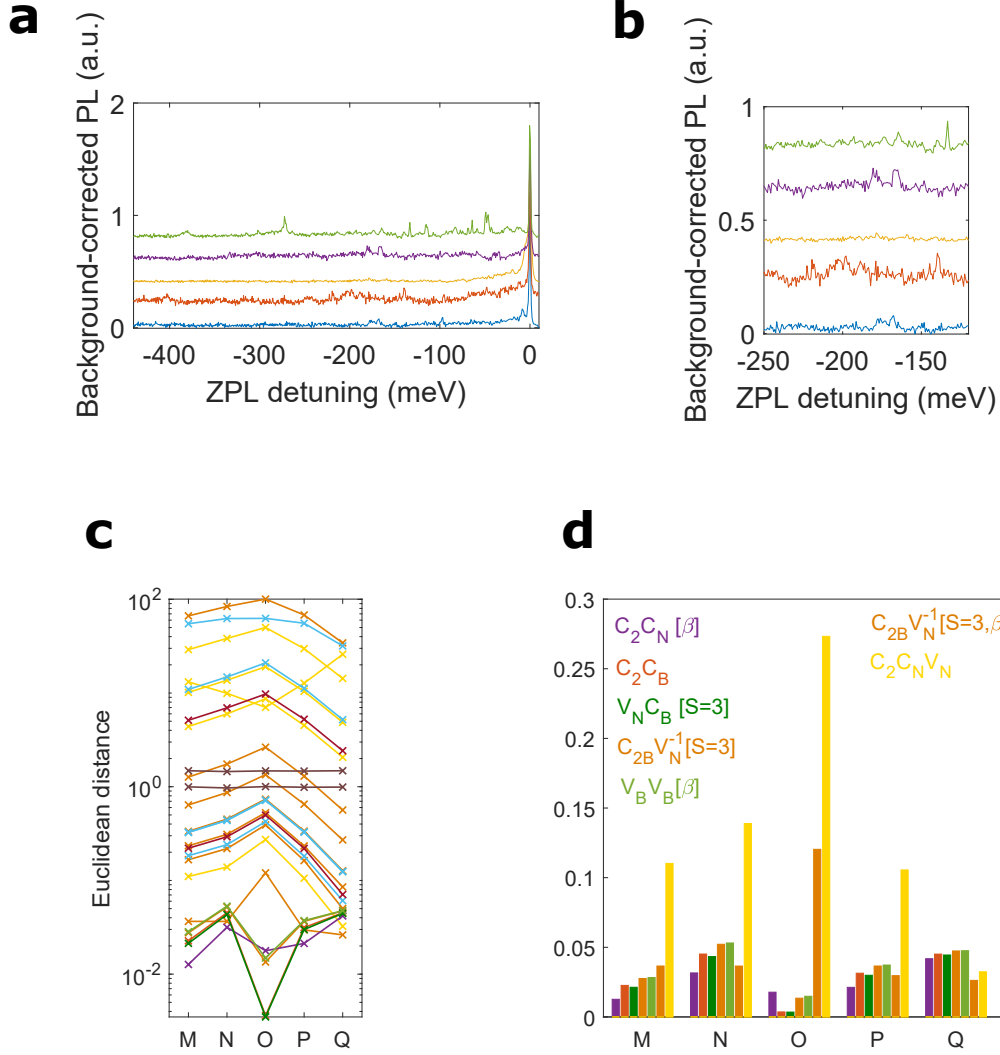


FIG. 16. **Low-temperature photoluminescence of luminescent centres not belonging to group I.** (a) Photoluminescence line shapes at  $T = 10$  K under 2.37 eV excitation, shifted vertically for clarity. The spectra from bottom to top correspond to Emitter M to Emitter Q, given by the x axis in (c). (b) Optical PSB of the luminescent centres shown in (a) with corresponding colors, shifted vertically for clarity. (c) Euclidean distance for Emitter M up to Emitter Q, with corresponding spectra shown in (a) from bottom to top. (d) Histograms of Emitter M to Emitter Q. The colors correspond to the defect transitions given by the legend. All line shapes are background corrected as outlined in Supplementary Information V and more details are given in the main text.

M	N	O	P	Q
2.0696	2.0139	2.1883	2.1210	2.1199

TABLE IV. Zero-phonon line energies (in electron-volt) of Emitter M to Q.

## XI. OPTICAL CHARACTERISATION

For optical characterisation, we use an objective (details below) to focus a laser onto the sample. For photoluminescence (PL), we use a continuous-wave (CW) laser with a photon energy of 2.37 eV. A helium flow cryostat is used for the low temperature measurements.

For PLE measurements at 10 K, we use a supercontinuum white light laser (78 MHz repetition rate) which is filtered down to a bandwidth of  $\sim 1$  nm with a tunable laser line filter. In order to compensate for intensity changes at different excitation wavelengths, we adjust the integration time of the spectrometer (see Supplementary Information VIII). For both photoluminescence (PL) and PLE measurements, the collected light is filtered by a longpass dichroic mirror (550 nm) and a 550 nm longpass filter. The filtered light is focused on the input slit of a spectrometer where the spectrum is obtained. The grating and detector information are given below.

For room temperature PL measurements, a 50X objective ( $NA = 0.6$ ), a 150 lines/mm grating, and an EMCCD are used. The low-temperature PL and PLE experiments are performed using a home-made confocal microscope with a 50X objective ( $NA = 0.42$ ), a 500 lines/mm grating, and a CCD detector. Furthermore, a spatial filter is used in front of the spectrometer for low-temperature measurements.

## XII. MODELLING PHONON EFFECTS IN PHOTOLUMINESCENCE EMISSION FROM LUMINESCENCE CENTERS

### A. The model Hamiltonian

We model the studied defect complex as a two level system (TLS) with ground state  $|g\rangle$  and excited state  $|e\rangle$ , with splitting  $\omega_e$  ( $\hbar = 1$ ). The TLS is driven by a continuous wave laser with a frequency  $\omega_L$  and Rabi coupling  $\Omega$ . The emitter couples to both a vibrational and optical environment, characterised by the Hamiltonian [18]:

$$H(t) = \omega_e |e\rangle\langle e| + \Omega \cos(\omega_L t) \sigma_x + |e\rangle\langle e| \sum_{\mathbf{k}} g_{\mathbf{k}} (b_{\mathbf{k}}^\dagger + b_{-\mathbf{k}}) + \sigma_x \sum_l (h_l^* a_l^\dagger + h_l a_l) + \sum_l \omega_l a_l^\dagger a_l + \sum_{\mathbf{k}} \nu_{\mathbf{k}} b_{\mathbf{k}}^\dagger b_{\mathbf{k}}, \quad (8)$$

where we have defined  $a_l^\dagger$  as the creation operator for a photon with energy  $\omega_l$ , and  $b_{\mathbf{k}}^\dagger$  as the creation operator for a phonon with energy  $\nu_{\mathbf{k}}$  and wavevector  $\mathbf{k}$ . We have also introduced the system operators  $\sigma_x = \sigma^\dagger + \sigma$  and  $\sigma = |g\rangle\langle e|$ . The coupling to the vibrational and electromagnetic environments are characterised by their respective spectral densities: for the optical environment we make the standard quantum optics approximation that the coupling constants  $h_l$  are frequency independent, such that  $J_{\text{EM}}(\omega) \approx \frac{\Gamma}{2\pi}$ , where  $\Gamma$  is the emission rate of the optical transition; the phonon spectral density takes the form  $J_{\text{Ph}}(\nu) = \sum_{\mathbf{k}} S_{\mathbf{k}} \delta(\nu - \nu_{\mathbf{k}})$  where  $S_{\mathbf{k}} = \omega_{\mathbf{k}}^2 |g_{\mathbf{k}}|^2$  are the partial Huang-Rhys parameters, and contain contributions from phonons calculated through *ab initio* methods and those fitted to the emission as detailed below.

We can simplify the above equation by making the rotating-wave approximation and moving to a frame rotating with respect to the laser frequency  $\omega_L$ , yielding the Hamiltonian:

$$H = \Delta |e\rangle\langle e| + \frac{\Omega}{2} \sigma_x + |e\rangle\langle e| \sum_{\mathbf{k}} g_{\mathbf{k}} (b_{\mathbf{k}}^\dagger + b_{\mathbf{k}}) + \sum_l (h_l^* \sigma a_l^\dagger e^{i\omega_L t} + h_l \sigma^\dagger a_l e^{-i\omega_L t}) + \sum_l \omega_l a_l^\dagger a_l + \sum_{\mathbf{k}} \nu_{\mathbf{k}} b_{\mathbf{k}}^\dagger b_{\mathbf{k}}, \quad (9)$$

where  $\Delta = \omega_e - \omega_L$  is the detuning between the driving field and the exciton transition. This Hamiltonian forms the starting point of our analysis of the dynamical and optical properties of the defect.

### B. Polaron theory for a driven emitter

In order to account for the strong coupling to the vibrational environment, we apply a polaron transformation to the global Hamiltonian, i.e. the unitary transformation  $\mathcal{U}_P = |e\rangle\langle e| \otimes B_+ + |g\rangle\langle g|$ , where  $B_{\pm} = \exp\left(\pm \sum_{\mathbf{k}} \nu_{\mathbf{k}}^{-1} g_{\mathbf{k}} (b_{\mathbf{k}}^\dagger - b_{-\mathbf{k}})\right)$  are displacement operators of the phonon environment [18, 25, 50]. This transformation dresses the excitonic states with vibrational modes of the phonon environment. In the polaron frame, the Hamiltonian may be written as  $H_P = H_0 + H_I^{\text{PH}} + H_I^{\text{EM}}$ , where

$$H_0 = \tilde{\Delta} |e\rangle\langle e| + \frac{\Omega_R}{2} \sigma_x + \sum_l \omega_l a_l^\dagger a_l + \sum_{\mathbf{k}} \nu_{\mathbf{k}} b_{\mathbf{k}}^\dagger b_{\mathbf{k}}, \quad (10)$$

$$H_I^{\text{PH}} = \frac{\Omega}{2} (\sigma_x B_x + \sigma_y B_y), \quad \text{and} \quad H_I^{\text{EM}} = \sum_l h_l^* \sigma B_+ a_l^\dagger e^{i\omega_L t} + \text{h.c.},$$

where we have introduced the phonon operators  $B_x = (B_+ + B_- - 2B)/2$ ,  $B_y = i(B_+ - B_-)/2$ , and the Frank-Condon factor of the phonon environment  $B = \text{tr}_B(B_{\pm} \rho_B) = \exp(-(1/2) \sum_{\mathbf{k}} \nu_{\mathbf{k}}^{-2} |g_{\mathbf{k}}|^2 \coth(\nu_{\mathbf{k}}/k_B T))$ , with the Gibbs state of the phonon environment in the polaron frame given by  $\rho_B = \exp(-\sum_{\mathbf{k}} \nu_{\mathbf{k}} b_{\mathbf{k}}^\dagger b_{\mathbf{k}}/k_B T) / \text{tr}(\exp(-\sum_{\mathbf{k}} \nu_{\mathbf{k}} b_{\mathbf{k}}^\dagger b_{\mathbf{k}}/k_B T))$ . Notice that the polaron transformation has dressed the operators in the light-matter coupling Hamiltonian, and renormalised the system parameters, such that  $\Omega_R = \Omega B$  and  $\tilde{\Delta} = \Delta - \sum_{\mathbf{k}} \nu_{\mathbf{k}}^{-1} g_{\mathbf{k}}^2$ .

The dynamics of the electronic states of the emitter are described by a 2<sup>nd</sup>-order Born-Markov master equation [53], where both the electromagnetic field and the transformed vibrational environment are perturbatively eliminated. The polaron transformation means that the vibrational interaction is included non-perturbatively in the interaction strength [18]. We can use the fact that only terms quadratic in field operators are non-zero when traced with a Gibbs state, so that there will be no cross-terms between the vibrational and electromagnetic dissipators, such that the master equation can be written in two parts:

$$\frac{\partial \rho(t)}{\partial t} = -i \left[ \tilde{\Delta} |e\rangle\langle e| + \frac{\Omega}{2} \sigma_x, \rho(t) \right] + \mathcal{K}_{\text{PH}}[\rho(t)] + \frac{\Gamma}{2} L_{\sigma}[\rho(t)] + \frac{\gamma}{2} L_{\sigma^\dagger \sigma}, \quad (11)$$

where  $\rho(t)$  is the reduced state of the emitter,  $L_\sigma[\rho] = 2\sigma\rho\sigma^\dagger - \{\sigma^\dagger\sigma, \rho\}$  is the Lindblad form dissipator for the electromagnetic environment, and similarly  $\mathcal{K}_{\text{PH}}$  describes the dissipation due to the vibrational environment. Note that we have also included a source of homogeneous broadening given by rate  $\gamma$ , to account for experimental imperfections and other dephasing mechanisms such as charge noise. For the optical dissipator, we refer the reader to standard texts in quantum optics for the derivation of the optical component [53], in the following section we outline the derivation of the phonon dissipator.

### 1. Deriving the phonon dissipator

Considering only the coupling to the vibrational modes, we move into the interaction picture with respect to the Hamiltonian  $H_0$ , the interaction term becomes:

$$H_I^{\text{PH}}(t) = \frac{\Omega}{2}[\sigma_x(t)B_x(t) + \sigma_y(t)B_y(t)], \quad (12)$$

where the interaction picture system operators are given by:

$$\begin{aligned} \sigma_x(t) &= \eta^{-2} \left[ \tilde{\Delta}\Omega_R(1 - \cos(\eta t))\sigma_z + (\Omega_R^2 + \tilde{\Delta}^2 \cos(\eta t))\sigma_x + \tilde{\Delta}\eta \sin(\eta t)\sigma_y \right], \\ \sigma_y(t) &= \eta^{-1} \left( \Omega_R \sin(\eta t)\sigma_z + \eta \cos(\eta t)\sigma_y - \tilde{\Delta} \sin(\eta t)\sigma_x \right), \end{aligned} \quad (13)$$

and we have defined the generalised Rabi frequency  $\eta = \sqrt{\tilde{\Delta}^2 + \Omega_R^2}$ . The interaction picture bath operators are found as  $B_{x/y}(t) = e^{iH_0 t} B_{x/y} e^{-iH_0 t}$ , with  $B_{x/y}$  defined above. In the Schrödinger picture and making the Born-Markov approximation in the polaron frame [53], the dissipator describing the electron-phonon interaction is given by:

$$\mathcal{K}_{\text{PH}}[\rho(t)] = -\frac{\Omega^2}{4} \int_0^\infty ([\sigma_x, \sigma_x(-\tau)\rho(t)]\Lambda_{xx}(\tau) + [\sigma_y, \sigma_y(-\tau)\rho(t)]\Lambda_{yy}(\tau) + \text{h. c.}) d\tau, \quad (14)$$

where we have and introduced the phonon bath correlation functions as  $\Lambda_{xx}(\tau) = \langle B_x(\tau)B_x \rangle = B^2(e^{\varphi(\tau)} + e^{-\varphi(\tau)} - 2)$ ,  $\Lambda_{yy}(\tau) = \langle B_y(\tau)B_y \rangle = B^2(e^{\varphi(\tau)} - e^{-\varphi(\tau)})$  which quantify the response of the phonon environment to the exciton dynamics. Taking the continuum limit over the phonon modes, these correlation functions can be described in terms of the polaron frame propagator  $\varphi(\tau) = \int_0^\infty d\nu \nu^{-2} J(\nu) [\coth(\nu/2k_B T) \cos(\nu\tau) - i \sin(\nu\tau)]$ . We can simplify the form of the master equation by evaluating the integrals over  $\tau$ , leading to:

$$\mathcal{K}_{\text{PH}}[\rho_s(t)] = -\frac{\Omega^2}{4} ([\sigma_x, \chi_x \rho_s(t)] + [\sigma_y, \chi_y \rho_s(t)] + \text{h. c.}), \quad (15)$$

where we have introduced the rate operators:

$$\chi_x = \int_0^\infty \sigma_x(-\tau)\Lambda_{xx}(\tau)d\tau = \frac{1}{\eta^2} [\Delta\Omega_r(\Gamma_0^x - \Gamma_c^x)\sigma_z + (\Omega_r^2\Gamma_0^x + \Delta^2\Gamma_c^x)\sigma_x + \Delta\eta\Gamma_s^x\sigma_y], \quad (16)$$

$$\chi_y = \int_0^\infty \sigma_y(-\tau)\Lambda_{yy}(\tau)d\tau = \frac{1}{\eta} [\Omega_r\Gamma_s^y\sigma_z - \Delta\Gamma_s^y\sigma_x + \eta\Gamma_c^y\sigma_y], \quad (17)$$

and defined the terms  $\Gamma_0^a = \int_0^\infty \Lambda_{aa}(\tau)d\tau$ ,  $\Gamma_c^a = \int_0^\infty \Lambda_{aa}(\tau) \cos(\eta\tau)d\tau$ ,  $\Gamma_s^a = \int_0^\infty \Lambda_{aa}(\tau) \sin(\eta\tau)d\tau$ , with  $a \in \{x, y\}$ . We may understand these terms as the rates at which transitions occur between the eigenstates of the system (i.e. the dressed states) induced by phonons. Qualitatively,  $\Gamma_s^a$  and  $\Gamma_c^a$  describe processes where a polaron is formed during excitation of the emitter, resulting in an exchange of energy with the environment. In contrast,  $\Gamma_0^a$  leads to no net exchange of energy, inducing a pure dephasing type process.

Since we are operating in the polaron frame, the above master equation is non-perturbative in the electron-phonon coupling strength, capturing strong-coupling and non-Markovian influences in the lab frame, despite having made a Born Markov approximation. This provides us with a simple, intuitive, and computationally straight-forward method for describing exciton dynamics in a regime where a standard weak coupling master equation would break down [18].

### C. Correlation functions and spectra for a driven emitter

We are interested in understanding the impact that phonon coupling has on the PLE spectrum, which can be calculated from the first-order correlation function  $g^{(1)}(t, \tau)$ . As shown in Ref. [24], the first-order correlation function in the polaron frame for the emitter is written in terms of the polaronic dipole operator  $\underline{\sigma} = \sigma B_+$ , that is, the correlation function is  $g_0^{(1)}(t, \tau) = \langle B_-(t + \tau) \sigma^\dagger(t + \tau) B_+(t) \sigma(t) \rangle$ . In general,  $B_\pm$  are many-body displacement operators that do not commute with system operators. However, in the regime that the polaron master equation is valid at second-order, we can factor this correlation function in the Born approximation, such that  $g_0^{(1)}(t, \tau) \approx \mathcal{G}(\tau) g_{\text{opt}}^{(1)}(t, \tau)$ . There are two terms in this expression, the correlation function for the scattered field  $g_{\text{opt}}^{(1)}(t, \tau) = \langle \sigma^\dagger(t + \tau) \sigma(t) \rangle$  describing the purely electronic transitions, and the phonon correlation function  $\mathcal{G}(\tau) = \langle B_-(\tau) B_+ \rangle = B^2 \exp(\varphi(\tau))$  which accounts for the relaxation of the phonon environment. This factorisation allows us to split the emission spectrum into two components  $S(\omega) = S_{\text{opt}}(\omega) + S_{\text{SB}}(\omega)$ , where  $S_{\text{opt}}(\omega) = \text{Re}[B^2 \int_0^\infty dt \int_0^\infty g_{\text{opt}}^{(1)}(t, \tau) e^{i\omega\tau} d\tau]$  corresponds to purely optical transitions, and  $S_{\text{SB}}(\omega) = \text{Re}[\int_0^\infty dt \int_0^\infty (\mathcal{G}(\tau) - B^2) g_{\text{opt}}^{(1)}(t, \tau) e^{i\omega\tau} d\tau]$  is attributed to non-Markovian phonon relaxation during the emission process, and leads to the emergence of a phonon sideband [54].

- 
- [1] I. Aharonovich, D. Englund, and M. Toth, Solid-state single-photon emitters, *Nature Photonics* **10**, 631 (2016).
- [2] T. T. Tran, K. Bray, M. J. Ford, M. Toth, and I. Aharonovich, Quantum emission from hexagonal boron nitride monolayers, *Nature Nanotechnology* **11**, 37 (2016).
- [3] J. L. O'Brien, A. Furusawa, and J. Vučković, Photonic quantum technologies, *Nature Photonics* **3**, 687 (2009).
- [4] A. Al-Juboori, H. Z. J. Zeng, M. A. P. Nguyen, X. Ai, A. Laucht, A. Solntsev, M. Toth, R. Malaney, and I. Aharonovich, Quantum key distribution using an integrated quantum emitter in hexagonal boron nitride (2023), arXiv:2302.06212.
- [5] C. L. Degen, F. Reinhard, and P. Cappellaro, Quantum sensing, *Rev. Mod. Phys.* **89**, 035002 (2017).
- [6] N. Mendelson, D. Chugh, J. R. Reimers, T. S. Cheng, A. Gottscholl, H. Long, C. J. Mellor, A. Zettl, V. Dyakonov, P. H. Beton, S. V. Novikov, C. Jagadish, H. H. Tan, M. J. Ford, M. Toth, C. Bradac, and I. Aharonovich, Identifying carbon as the source of visible single-photon emission from hexagonal boron nitride, *Nature Materials* **20**, 321 (2021).
- [7] M. Fischer, J. M. Caridad, A. Sajid, S. Ghaderzadeh, M. Ghorbani-Asl, L. Gammelgaard, P. Bøggild, K. S. Thygesen, A. V. Krashennnikov, S. Xiao, M. Wubs, and N. Stenger, Controlled generation of luminescent centers in hexagonal boron nitride by irradiation engineering, *Science Advances* **7**, eabe7138 (2021).
- [8] C. Jara, T. Rauch, S. Botti, M. A. L. Marques, A. Norambuena, R. Coto, J. E. Castellanos-Águila, J. R. Maze, and F. Munoz, First-principles identification of single photon emitters based on carbon clusters in hexagonal boron nitride, *The Journal of Physical Chemistry A* **125**, 1325 (2021).
- [9] K. Li, T. J. Smart, and Y. Ping, Carbon trimer as a 2 eV single-photon emitter candidate in hexagonal boron nitride: A first-principles study, *Phys. Rev. Mater.* **6**, L042201 (2022).
- [10] A. Sajid and K. S. Thygesen,  $V_N C_B$  defect as source of single photon emission from hexagonal boron nitride, *2D Materials* **7**, 031007 (2020).
- [11] S. A. Tawfik, S. Ali, M. Fronzi, M. Kianinia, T. T. Tran, C. Stampfl, I. Aharonovich, M. Toth, and M. J. Ford, First-principles investigation of quantum emission from hBN defects, *Nanoscale* **9**, 13575 (2017).
- [12] C. Linderålv, W. Wiczorek, and P. Erhart, Vibrational signatures for the identification of single-photon emitters in hexagonal boron nitride, *Phys. Rev. B* **103**, 115421 (2021).
- [13] P. Auburger and A. Gali, Towards ab initio identification of paramagnetic substitutional carbon defects in hexagonal boron nitride acting as quantum bits, *Phys. Rev. B* **104**, 075410 (2021).
- [14] H. Schauffert, J. C. Stewart, S. Ali, S. Walser, H. Hörner, A. S. Prasad, V. Babenko, Y. Fan, D. Eder, K. S. Thygesen, S. Hofmann, B. C. Bayer, and S. M. Skoff, Characteristics of quantum emitters in hexagonal boron nitride suitable for integration with nanophotonic platforms (2023), arXiv:2210.11099.
- [15] J. A. Preuss, D. Groll, R. Schmidt, T. Hahn, P. Machnikowski, R. Bratschitsch, T. Kuhn, S. M. de Vasconcellos, and D. Wigger, Resonant and phonon-assisted ultrafast coherent control of a single hBN color center, *Optica* **9**, 522 (2022).
- [16] M. Nguyen, S. Kim, T. T. Tran, Z.-Q. Xu, M. Kianinia, M. Toth, and I. Aharonovich, Nanoassembly of quantum emitters in hexagonal boron nitride and gold nanospheres, *Nanoscale* **10**, 2267 (2018).
- [17] T. Vogl, R. Lecamwasam, B. C. Buchler, Y. Lu, and P. K. Lam, Compact cavity-enhanced single-photon generation with hexagonal boron nitride, *ACS Photonics* **6**, 1955 (2019).
- [18] A. Nazir and D. P. S. McCutcheon, Modelling exciton-phonon interactions in optically driven quantum dots, *Journal of Physics: Condensed Matter* **28**, 103002 (2016).
- [19] M. A. Feldman, A. Puzos, L. Lindsay, E. Tucker, D. P. Briggs, P. G. Evans, R. F. Haglund, and B. J. Lawrie, Phonon-induced multicolor correlations in hBN single-photon emitters, *Phys. Rev. B* **99**, 020101 (2019).
- [20] M. K. Boll, I. P. Radko, A. Huck, and U. L. Andersen, Photophysics of quantum emitters in hexagonal boron-nitride nano-flakes, *Opt. Express* **28**, 7475 (2020).
- [21] L. J. Martínez, T. Pelini, V. Waselowski, J. R. Maze, B. Gil, G. Cassabois, and V. Jacques, Efficient single photon emission from a high-purity hexagonal boron nitride crystal, *Phys. Rev. B* **94**, 121405 (2016).
- [22] A. Sajid, J. R. Reimers, and M. J. Ford, Defect states in hexagonal boron nitride: Assignments of observed properties and prediction of properties relevant to quantum computation, *Phys. Rev. B* **97**, 064101 (2018).
- [23] M. K. Svendsen, S. Ali, N. Stenger, K. S. Thygesen, and J. Iles-Smith, Signatures of non-Markovianity in cavity-QED with color centers in 2D materials (2022), arXiv:2207.10630.
- [24] J. Iles-Smith, D. P. McCutcheon, A. Nazir, and J. Mørk, Phonon scattering inhibits simultaneous near-unity efficiency and indistinguishability in semiconductor single-photon sources, *Nature Photonics* **11**, 521 (2017).
- [25] J. Iles-Smith, D. P. McCutcheon, J. Mørk, and A. Nazir, Limits to coherent scattering and photon coalescence from solid-state quantum emitters, *Physical Review B* **95**, 201305 (2017).
- [26] A. Taghizadeh, U. Leffers, T. G. Pedersen, and K. S. Thygesen, A library of ab initio raman spectra for automated identification of 2d materials, *Nature Communications* **11**, 3011 (2020).
- [27] A. Bommer and C. Becher, New insights into nonclassical light emission from defects in multi-layer hexagonal boron nitride, *Nanophotonics* **8**, 2041 (2019).
- [28] T. T. Tran, C. Elbadawi, D. Totonjian, C. J. Lobo, G. Grosso, H. Moon, D. R. Englund, M. J. Ford, I. Aharonovich, and M. Toth, Robust multicolor single photon emission from point defects in hexagonal boron nitride, *ACS Nano* **10**, 7331 (2016).
- [29] T. Vogl, G. Campbell, B. C. Buchler, Y. Lu, and P. K. Lam, Fabrication and deterministic transfer of high-quality quantum emitters in hexagonal boron nitride, *ACS Photonics* **5**, 2305 (2018).

- [30] N. Mendelson, Z.-Q. Xu, T. T. Tran, M. Kianinia, J. Scott, C. Bradac, I. Aharonovich, and M. Toth, Engineering and tuning of quantum emitters in few-layer hexagonal boron nitride, *ACS Nano* **13**, 3132 (2019).
- [31] D. Wigger, R. Schmidt, O. Del Pozo-Zamudio, J. A. Preuß, P. Tonndorf, R. Schneider, P. Steeger, J. Kern, Y. Khodaei, J. Sperling, S. M. de Vasconcellos, R. Bratschitsch, and T. Kuhn, Phonon-assisted emission and absorption of individual color centers in hexagonal boron nitride, *2D Materials* **6**, 035006 (2019).
- [32] B. Krummheuer, V. M. Axt, and T. Kuhn, Theory of pure dephasing and the resulting absorption line shape in semiconductor quantum dots, *Phys. Rev. B* **65**, 195313 (2002).
- [33] G. Grosso, H. Moon, C. J. Ciccarino, J. Flick, N. Mendelson, L. Mennel, M. Toth, I. Aharonovich, P. Narang, and D. R. Englund, Low-temperature electron–phonon interaction of quantum emitters in hexagonal boron nitride, *ACS Photonics* **7**, 1410 (2020).
- [34] X. Li, G. D. Shepard, A. Cupo, N. Camporeale, K. Shayan, Y. Luo, V. Meunier, and S. Strauf, Nonmagnetic quantum emitters in boron nitride with ultranarrow and sideband-free emission spectra, *ACS Nano* **11**, 6652 (2017).
- [35] Z.-Q. Xu, C. Elbadawi, T. T. Tran, M. Kianinia, X. Li, D. Liu, T. B. Hoffman, M. Nguyen, S. Kim, J. H. Edgar, X. Wu, L. Song, S. Ali, M. Ford, M. Toth, and I. Aharonovich, Single photon emission from plasma treated 2D hexagonal boron nitride, *Nanoscale* **10**, 7957 (2018).
- [36] G. Cassabois, P. Valvin, and B. Gil, Hexagonal boron nitride is an indirect bandgap semiconductor, *Nature Photonics* **10**, 262 (2016).
- [37] Z.-Q. Xu, N. Mendelson, J. A. Scott, C. Li, I. H. Abidi, H. Liu, Z. Luo, I. Aharonovich, and M. Toth, Charge and energy transfer of quantum emitters in 2D heterostructures, *2D Materials* **7**, 031001 (2020).
- [38] R. N. E. Malein, P. Khatri, A. J. Ramsay, and I. J. Luxmoore, Stimulated emission depletion spectroscopy of color centers in hexagonal boron nitride, *ACS Photonics* **8**, 1007 (2021).
- [39] N. R. Jungwirth and G. D. Fuchs, Optical absorption and emission mechanisms of single defects in hexagonal boron nitride, *Physical Review Letters* **119**, 057401 (2017).
- [40] M. Kianinia, B. Regan, S. A. Tawfik, T. T. Tran, M. J. Ford, I. Aharonovich, and M. Toth, Robust solid-state quantum system operating at 800 K, *ACS Photonics* **4**, 768 (2017).
- [41] T. T. Tran, C. Zachreson, A. M. Berhane, K. Bray, R. G. Sandstrom, L. H. Li, T. Taniguchi, K. Watanabe, I. Aharonovich, and M. Toth, Quantum emission from defects in single-crystalline hexagonal boron nitride, *Phys. Rev. Applied* **5**, 034005 (2016).
- [42] P. Khatri, I. J. Luxmoore, and A. J. Ramsay, Phonon sidebands of color centers in hexagonal boron nitride, *Phys. Rev. B* **100**, 125305 (2019).
- [43] A. Kumar, Çağlar Samaner, C. Cholsuk, T. Matthes, S. Paçal, Y. Oyun, A. Zand, R. J. Chapman, G. Saerens, R. Grange, S. Suwanna, S. Ateş, and T. Vogl, Polarization dynamics of solid-state quantum emitters (2023), arXiv:2303.04732.
- [44] C. Li, N. Mendelson, R. Ritika, Y. Chen, Z.-Q. Xu, M. Toth, and I. Aharonovich, Scalable and deterministic fabrication of quantum emitter arrays from hexagonal boron nitride, *Nano Letters* **21**, 3626 (2021).
- [45] X. Xu, Z. O. Martin, D. Sychev, A. S. Lagutchev, Y. P. Chen, T. Taniguchi, K. Watanabe, V. M. Shalaev, and A. Boltasseva, Creating quantum emitters in hexagonal boron nitride deterministically on chip-compatible substrates, *Nano Letters* **21**, 8182 (2021).
- [46] J. Enkovaara, C. Rostgaard, J. J. Mortensen, J. Chen, M. Dułak, L. Ferrighi, J. Gavnholt, C. Glinsvad, V. Haikola, H. Hansen, *et al.*, Electronic structure calculations with GPAW: a real-space implementation of the projector augmented-wave method, *Journal of Physics: Condensed Matter* **22**, 253202 (2010).
- [47] J. P. Perdew, K. Burke, and M. Ernzerhof, Generalized gradient approximation made simple, *Physical review letters* **77**, 3865 (1996).
- [48] G. Levi, A. V. Ivanov, and H. Jonsson, Variational calculations of excited states via direct optimization of orbitals in DFT, *Faraday Discussions* (2020).
- [49] F. Bertoldo, S. Ali, S. Manti, and K. S. Thygesen, Quantum point defects in 2D materials - the QPOD database, *npj Computational Materials* **8**, 56 (2022).
- [50] D. P. McCutcheon and A. Nazir, Quantum dot Rabi rotations beyond the weak exciton–phonon coupling regime, *New Journal of Physics* **12**, 113042 (2010).
- [51] C. Cholsuk, S. Suwanna, and T. Vogl, Tailoring the emission wavelength of color centers in hexagonal boron nitride for quantum applications, *Nanomaterials* **12**, 2427 (2022).
- [52] Background correction, [https://in.mathworks.com/matlabcentral/fileexchange/27429-background-correction?s\\_tid=FX\\_rc2\\_behav](https://in.mathworks.com/matlabcentral/fileexchange/27429-background-correction?s_tid=FX_rc2_behav) (2012), accessed: 30.03.2022.
- [53] H. Breuer, F. Petruccione, and S. Petruccione, *The Theory of Open Quantum Systems* (Oxford University Press, 2002).
- [54] A. J. Brash, J. Iles-Smith, C. L. Phillips, D. P. McCutcheon, J. O’Hara, E. Clarke, B. Royall, L. R. Wilson, J. Mørk, M. S. Skolnick, *et al.*, Light scattering from solid-state quantum emitters: beyond the atomic picture, *Physical Review Letters* **123**, 167403 (2019).